THEORETICAL STUDIES OF POLY(FERROCENYLSILANES): CHAIN CONFIGURATION AND SELF-ASSEMBLY

By

RUI ZHANG, B.Sc.

A Thesis
Submitted to the School of Graduate Studies
in Partial Fulfilment of the Requirements
for the Degree
Master of Science

McMaster University
©Copyright by Rui Zhang, 2006.

MASTER OF SCIENCE (2006) McMaster University
(Physics) Hamilton, Ontario

TITLE: THEORETICAL STUDIES OF POLY(FERROCENYLSILANES): CHAIN CONFIGURATION AND SELF-ASSEMBLY

AUTHOR: Rui Zhang,B.Sc.(Tsinghua University, P.R. China)

SUPERVISOR: Dr. A.-C. Shi

NUMBER OF PAGES: 1, 74

Abstract

This thesis summarizes theoretical results of two projects on the investigation of a novel organometallic polymer, the polyferrocenylsilanes(PFS). The study is carried out in collaboration with the experimental groups of Prof. Manners and Prof. Winnik at the Department of Chemistry of University of Toronto.

In the first project, a rotational isomeric state (RIS) model is applied to study the configurational statistics of an ideal polyferrocenyldimethylsilane (PFDMS) chain: $Fc[Fe(C_5H_4)_2SiMe_2]_nH$ ($Fc = Fe(C_5H_5)(C_5H_4)$). The necessary conformation energies are derived from the molecular mechanics study of oligomeric (n=1,2) models for PFDMS reported by O'Hare et al.(*J. Am. Chem. Soc.* **1996,** *118,* 7578). In particular, pseudoatom and pseudobonds are introduced to describe the RIS chain of PFDMS, consistent with the special molecular geometry of the repeating ferrocene and organosilane units. The mean square unperturbed dimensions ($\langle r^2 \rangle_0$, $\langle R_g^2 \rangle_0$), the characteristic ratios $C_n(C_\infty)$ and the temperature coefficients $d \ln \langle r^2 \rangle_0 / dT$ of PFDMS are calculated. The results show that an ideal PFDMS chain has a relatively low value of C_∞ and fast convergence of C_n to C_∞ with increasing n, indicating a high static flexibility of this type of transition metal-containing polymer. The previously

unknown Kuhn length of PFDMS is obtained based on the calculated C_∞.

In the second project, by taking PFS-b-PDMS/alkane as a model system, general phase behaviours of the self-assembled micelles in dilute crystalline-coil copolymer solutions (solvents are selective for the coil blocks) are investigated. Three types of aggregates — lamellar, rodlike and tubular micelles are studied based on the existing experimental observations. The computation results reveal three types of phase diagrams, namely, lamella-tube-rod phase diagrams with or without a triple point and lamella-rod phase diagrams. It is shown that lamella-tube-rod morphological transitions can be induced by changing the coil/crystalline block ratio or the temperature. Possible improvement of the theory and the current challenges of studying PFS-b-PDMS self-assembly in alkane solvents for both theories and experiments are discussed.

Contents

List of Tables

List of Figures

Acknowledgements

I would like to first acknowledge my supervisor Professor An-Chang Shi. Without his patient and comprehensive guidance on my research, I could not have the chance to obtain the interesting results shown in this thesis. I am also very much indebted to my supervisor An-Chang Shi for his patient modification of my awkward draft containing many language mistakes and sentences which could be better written.

Many thanks to my committee, Professor Paul Higgs, Professor Cecile Fradin and Professor Kari Dalnoki-Veress, for their valuable comments and suggestions to my research subject. I would especially like to thank Kari, for his willingness in reading my thesis and acting as an examiner on my defence.

I am indebted to Professor Ian Manners and Professor Mitchell A. Winnik at University of Toronto for their trust and encouragement through my research. This work could not be done without many important experimental data provided by them.

I would like to thank the members of our group, David M. Cooke, Karim Jaffer, Issei Nakamura, and Youhai Sun, for the helpful discussions with them. Also, thanks to my best friends, Fanlong Ning, Fei Lin, Zhuowei Zhou, Jiajia Zhou, and Yang Zhao, for their much help to my study and daily life.

Special thanks to my parents, for their support and encouragement in the weekly phone calls, motivating me to overcome the difficulties encountered in study and research.

Chapter 1

Introduction

Polyferrocenylsilanes represent a recently established, readily accessible class of transition metal-containing polymers consisting of alternating ferrocene and organosilane units. High molecular weight, soluble samples of these materials were first prepared in the early 1990's by thermal ring-opening polymerization (ROP) using silicon-bridged ferrocenophanes[1]. More recently living anionic and transition metal-catalyzed ROP methodologies have been developed, which permit unprecedented access to controlled polymer architectures (e.g., block copolymers) with transition metals in the main chain. Polyferrocenylsilane homopolymers and block copolymers offer exciting opportunities in materials and supramolecular science and for nanostructure applications[2].

As one prototypical example of polymers containing transition metals in the main chain, polyferrocenylsilanes are attracting growing attentions as processable materials with novel physical (e.g., redox, magnetic, electrical and morphological) and chemical (e.g., catalytic and preceramic) properties[2, 3]. Some interesting properties of

polyferrocenylsilanes have been reported. For example, polyferrocenylsilanes possess interesting hole transport properties and partial oxidation leads to a 10^{10} fold increase in electrical conductivity up to semiconductor values (ca. $10^{-3} - 10^{-4}$ Scm^{-1})[4].

In this thesis, we summarize theoretical results of two projects on the investigation of the chain configuration of polyferrocenylsilanes and the solution self-assembly of polyferrocenylsilane block copolymers. The study is carried out in collaboration with the experimental groups of Prof. Manners and Prof. Winnik at the Department of Chemistry of University of Toronto. In previous experiments performed by Manners et al., interesting configurational and self-assembly properties of polyferrocenylsilanes have been revealed as described below.

In THF solvents, poly(ferrocenyldimethylsilanes) possess a more compact random-coil conformation relative to polystyrene, and this accounts for the underestimation of molecular weight by conventional gel-permeation chromatograph (GPC) methods using polystyrene standards[5]. Although this observation by Manners et al. qualitatively shows polyferrocenylsilane chains are flexible, the quantitative results of the chain configuration are still unknown. To resolve this problem, we construct a rotational isomeric state model to compute several important configuratioanl parameters for polyferrocenylsilanes, such as the radius of gyration and the Kuhn length. The results confirm that polyferrocenylsilanes are of high static flexibility at high temperature. This project is summarized in chapter 2.

For the solution assembly of polyferrocenylsilane block copolymers, Manners et al. have observed intriguing micellar morphologies. The organometallic–inorganic diblock copolymer poly(ferrocenylsilane-b-dimethylsiloxane) (PFS-b-PDMS) with large

PDMS/PFS block ratio unexpectedly forms long cylindrical micelles rathen than spherical micelles in a variety of PDMS-selective alkane solvents[6, 7, 8, 9]. Since in the experiments the temperatures were all below the melting temperature T_m of PFS, the crystallinity of PFS has been taken as the driving force of the formation of non-spherical micelles[6]. However, theoretical understanding of many aspects of the self-assembly in the PFS-b-PDMS/alkane system is still lacking. In chapter 3, we summarize the preliminary results on the investigation of the phase behaviours of crystalline-coil diblock copolymers in the coil-selective solvents by taking PFS-b-PDMS/alkane as a model system.

Chapter 2

Configurational Statistics of An Ideal PFDMS Chain

2.1 Introduction

The rotational isomeric state (RIS) model is widely used to study the conformational properties of real polymer chains[10, 11, 12]. Over the past four decades, RIS models for hundreds of polymer structures have been developed and published[12]. The general RIS calculation includes the following steps[12]: (1) identify all skeletal bonds around which rotation is possible under the chosen conditions; (2) for each of these bonds, analyze the interactions of short range that determine its conformational behaviour. Usually one finds that the torsion angles of the bonds in question can assume only relatively narrow domains and one identifies these domains with rotational isomeric states. The location of these states determines the geometry of those "rotational isomers" selected to represent the totality of conformations avail-

able to the polymer; (3) determine the energy or free energy of the selected rotational isomers and compute the statistical weights to obtain the statistical weight matrices (U-matrices); (4) compute the configurational properties of the polymer. Generally speaking, it is relatively easy to determine the geometrical parameters (bond lengths and angles) of a real chain to high accuracy, thus, the reliability of the RIS calculation is largely determined by the accuracy of the (local) conformation energies which dictate the statistical weight matrices.

In this chapter, the configurational properties of an ideal polyferrocenyldimethylsilane (PFDMS) chain is studied in the framework of the RIS model. The necessary local conformation energies (short-range interaction energies) are obtained from the extensible systematic forcefield (ESFF) calculations reported by O'Hare et al.[13]. Polyferrocenylsilanes represent a recently established, readily accessible class of transition metal-containing polymers consisting of alternating ferrocene and organosilane units. These polymers are differentiated by the two side groups (R,R′) covalently bonded to the silicon atom, which could be alkyl, aryl, alkoxy, aryloxy and amino substitutes[2]. For PFDMS, $R = R' = CH_3(Me)$. The first synthesis of high molecular weight polyferrocenylsilanes was performed by thermal ring-opening polymerization (ROP) using silicon-bridged ferrocenophanes by Manners and coworkers[1]. In recent years, it has been shown that polyferrocenylsilanes have interesting potential in materials science, self-assembly and nanoscience[2].

This chapter is organized as follows: In section 2.2, we analyze the molecular geometry of PFDMS. We show that the introduction of the pseudoatom and pseudobonds permits the classical RIS chain description of PFDMS. In section 2.3, we summarize

the low-energy conformations of the PFDMS oligomers reported by O'Hare et al.[13] and construct the RIS ensemble for PFDMS, where the strong interdependence of the torsion angles leads to large-size statistical weight matrices. The main results are given in section 2.4. Configurational properties of an ideal polymer chain, including the mean square end-to-end distances $\langle r^2 \rangle_0$, the mean square radiuses of gyration $\langle R_g^2 \rangle_0$, the characteristic ratios $C_n(C_\infty)$ and the temperature coefficients $d \ln \langle r^2 \rangle_0 / dT$ are calculated. Discussions are given in section 2.5.

2.2 Molecular Geometry

2.2.1 Analysis

Usually, the backbone of a real polymer is a good description of the RIS chain, where bond lengths and bond angles of the backbone are taken as constants, leaving the torsion angles as the only degrees of freedom responsible for the various chain configurations. For example, the RIS chain of polydimethysiloxanes (PDMS) can be taken as $\cdots - \mathrm{Si} - \mathrm{O} - \mathrm{Si} - \mathrm{O} - \cdots$, which is the same as the PDMS backbone[10]. However, the PFDMS chain is an exception because of the special molecular geometry of the ferrocene and organasilane units. The unconventional chemical bonds of PFDMS lead to the following geometrical restrictions:

(1) The two cyclopentadienyl (Cp) rings within one ferrocene are strictly parallel (Figure 2.1). However, relative rotation of the two rings is permitted. Therefore the bond angle ∠C-Fe-C in the backbone $(\mathrm{C} - \mathrm{Fe} - [\mathrm{C} - \mathrm{Si} - \mathrm{C} - \mathrm{Fe}]_n - \mathrm{C})$ can not be

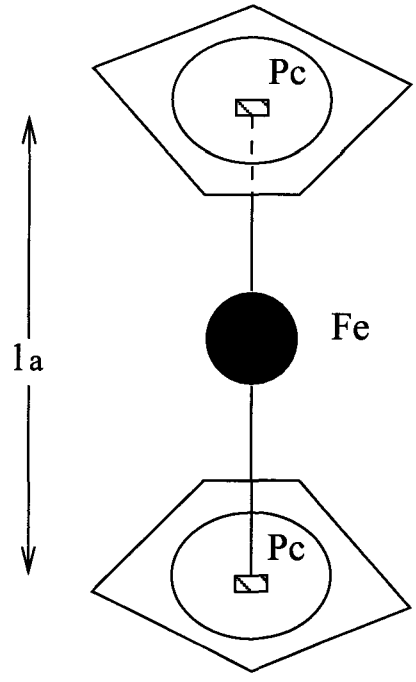

Figure 2.1: Schematic of the pseudobond Pc-Pc. Pc denotes the pseudoatom located at the center of the cyclopendadineyl ring. The length of this pseudobond is denoted as l_a.

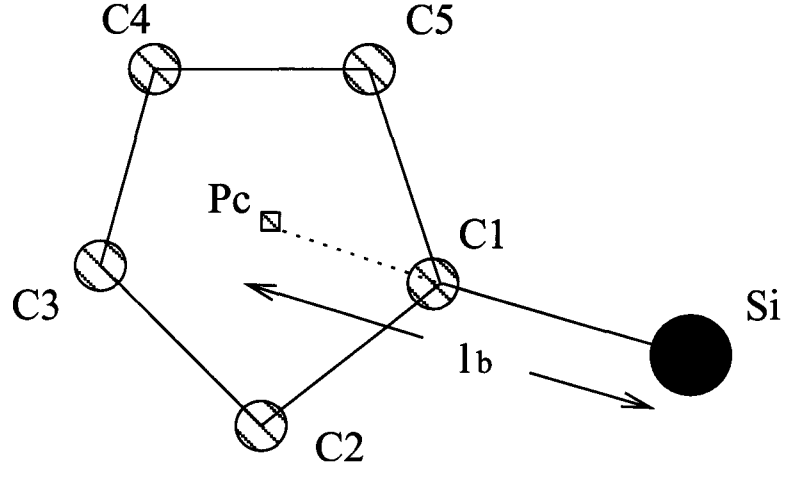

Figure 2.2: Schematic of the pseudobond Pc-Si. The length of this pseudobond is denoted as l_b.

bond type	Fe-C	C-C	C-Si	Pc-C
bond length(Å)	2.04	1.42	1.85	1.21
bond type	Fe-Pc	**Pc-Pc**	**Pc-Si**	
bond length(Å)	1.645	**3.29**	**3.06**	

Table 2.1: (Pseudo) bond lengths of PFDMS. Parameters from Manners et al.[14]

taken as a constant in the RIS model.

(2) The iron atom is at the middle of the segment connecting the centers of the two rings (Figure 2.1).

(3) The C-Si bond in the backbone is almost coplanar with the Cp ring (Figure 2.2). This property is not due to geometrical restrictions. Rather, it is based on experimental data [14] which indicates $\angle C_5\text{-}C_1\text{-}Si + \angle C_2\text{-}C_1\text{-}Si + \angle C_5\text{-}C_1\text{-}C_2$ is very close to 360°.

2.2.2 RIS Chain of PFDMS

We construct a RIS chain for the PFDMS by introducing the pseudoatom and pseudobonds as follows: The pseudoatom is located at the center of the cyclopentadienyl ring, denoted as "Pc". The two associated pseudobonds are Pc-Pc and Pc-Si bonds. With these definitions, a configuration of the PFDMS chain can be described by the configuration of a RIS chain $Pc - [Pc - Si - Pc]_n - Pc$ which is specified by $3n - 1$ torsion angles (Figure 2.3). The validity of this RIS model can be justified by the molecular geometrical analysis shown in subsection 2.2.1. The geometrical parameters are given in Table 2.1 and 2.2.

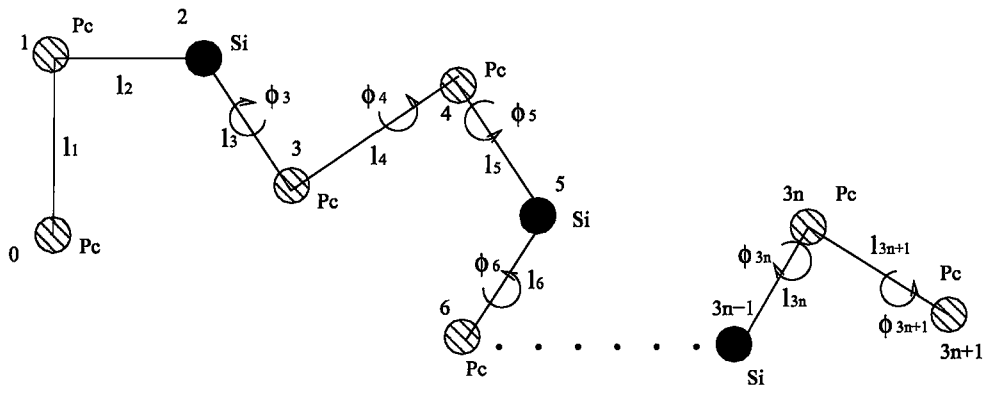

Figure 2.3: Schematic of the RIS chain of PFDMS. Pc is the pseudoatom. The chain configuration is determined by $3n-1$ torsion angles, labeled as $\Phi_3, \Phi_4, \ldots, \Phi_{3n+1}$, where Φ_i is the dihedral angle between the two planes defined by bond $i-2$, $i-1$ and $i-1$, i, respectively. Note that in this paper we determine the values of the torsion angles following Flory's rule (right-handed helices are generated by positive rotations)[10], e.g., all torsion angles are 0° for a perfect trans planar zigzag conformation, which is different from the rule (left-handed helices are generated by positive rotations) adopted by O'Hare et al[13].

angle type	Pc-Fe-Pc	**Pc-Pc-Si**	Fe-C-Si
angle (°)	180	**90**	128.5
angle type	Pc-C-Si	**Pc-Si-Pc**	
angle (°)	180	**107.6**	

Table 2.2: (Pseudo) bond angles of PFDMS. Parameters from Manners et al.[14]

2.3 Short-range Interactions

In this section, we discuss an important aspect of the RIS calculation for an ideal PFDMS chain, namely, the short-range interactions. As reported by O'Hare et al.[13], the conformational energies of PFDMS oligomers are almost exclusively determined by the non-bonding electrostatic interactions between the positively charged iron atoms and negatively charged Cp rings in the ferrocene units. In contrast, the energetic contribution from the organosilane units is much smaller. On the basis of such

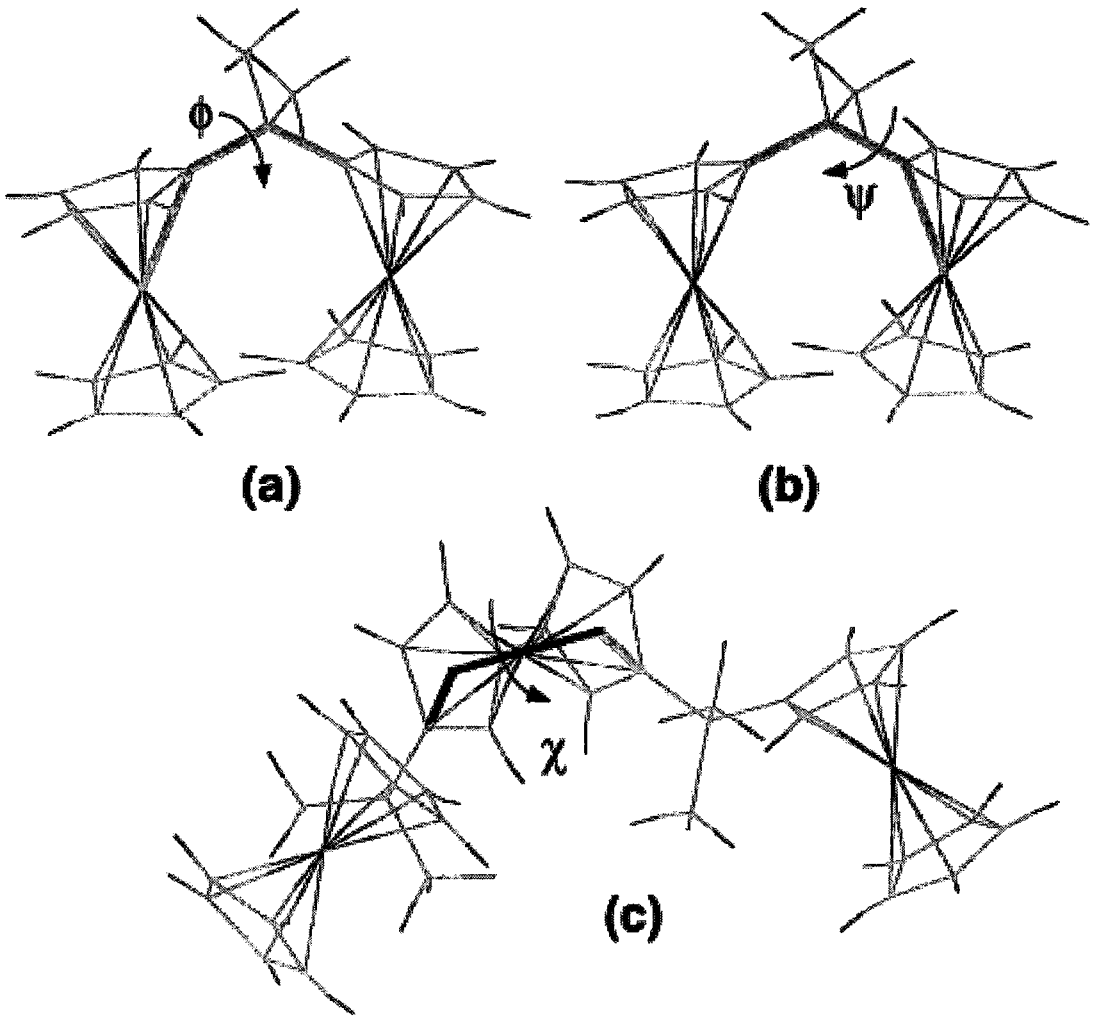

Figure 2.4: Schematic of the dimer and trimer conformations. The pictures are taken from O'Hare et al.[13]: (a)the angle ϕ in the dimer pair; (b)the angle ψ in the dimer pair; (c)the trimer angle χ.

energetic features, the first-order and second-order interactions of PFDMS, which constitute the short-range interactions, are defined as the interactions between two nearest-neighbour ferrocenes (dictated by two torsion angles) and the interactions between two second-nearest-neighbour ferrocenes (dictated by five torsion angles), respectively. Details of this approach are given below.

2.3.1 First-order Interactions

A dimer(n=1) contains two nearest-neighbour ferrocenes, whose relative positions are determined by two torsion angles ϕ and ψ (Figure 2.4a and 2.4b). Thus, the first-order interaction energy is a function of two torsion angles. Three symmetry-independent potential minima (Figure 2.5) were found by O'Hare et al.: (145°,20°), (110°,110°) and (13°,13°). Because the third minimum is 3.9Kcal/mol $\approx$ 5kT higher than the first minimum and 2.9Kcal/mol $\approx$ 3.5kT higher than the second minimum, it is excluded from our RIS ensemble. In the framework of the RIS calculation[10, 11], the first and second minimum lead to six distinct rotational isomeric states: (145°,20°), (20°,145°), (−145°,−20°), (−20°,−145°), (110°,110°) and (−110°,−110°). In what follows, when a higher-degree oligomer(n>1) is considered, one unit composed of two nearest-neighbour ferrocenes and the bridged organosilane unit is referred as a dimer unit. The pair of torsion angles in it is referred as a dimer pair. In the RIS calculation, the values of one dimer pair are derived from either the first or the second minimum shown above. To facilitate the following discussion, for the former or latter case, the dimer pair is referred as a type-I or type-II pair, respectively. For example,

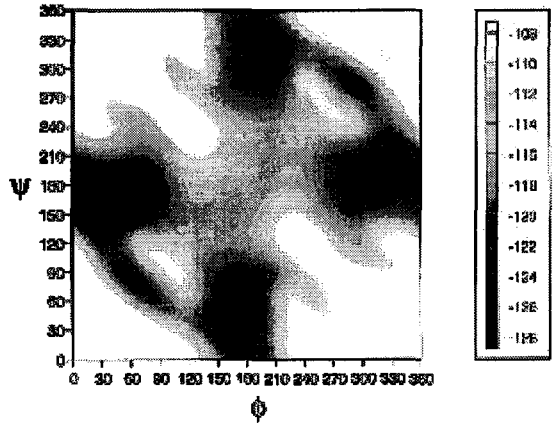

Figure 2.5: Plot of the dimer energy (Kcal/mol) as a function of the dimer pair ϕ and ψ. The picture is taken from O'Hare et al.[13].

(20°,145°) is a type-I pair and (−110°,−110°) is a type-II pair.

2.3.2 Second-order Interactions

A trimer(n=2) contains three ferrocenes and it is the smallest unit containing a pair of second-nearest-neighbour ferrocenes. Its conformation is determined by five torsion angles. Thus, the second-order interaction energy is a function of five torsion angles. Four of these angles are the same as the two dimer pairs of the trimer. The last (fifth) angle, χ (Figure 2.4c), denotes the angle through which the two C-Si bonds connected to the two Cp rings of the central ferrocene are twisted away from one another[13]. It is referred as a trimer angle. Analogous to the definition of a dimer unit, when a higher-degree oligomer(n>2) is considered, one unit composed of three sequential ferrocenes and the two bridged organosilane units is referred as a trimer unit. The conformation of a trimer unit is determined by two dimer pairs and one trimer angle.

The energy of a trimer unit can then be formally expressed as:

$$\begin{aligned} E(trimer) &= E(dimer1) + E(dimer2) + E'(trimer) \\ &= E(\phi_1, \psi_1) + E(\phi_2, \psi_2) + E'(\phi_1, \psi_1, \chi, \psi_2, \phi_2) \end{aligned} \tag{2.1}$$

where, the first two terms represent the first-order interactions and the third (last) term represents the second-order interactions.

For a trimer, there are 10 lowest-energy conformations. The studies of O'Hare et al. show that there are two features of these conformations[13].

First, as shown in subsection 2.3.1, six rotational isomeric states of the dimer pairs are determined based on the first-order interactions. Now, upon adding the second-order interactions to determine the low-energy trimers, we would expect that some deviation arises for the angle values of the dimer pairs in the low-energy trimers compared with the angle values of the dimer pairs included in the six rotational isomeric states mentioned above. The results of the ESFF calculation[13] show that such deviation is small. The average deviation is 7.2° and the largest deviation is 32°. Thus, for the RIS calculation performed in the current work, it is reasonable to choose six rotational isomeric states in total for the dimer pairs. Their values are consistent with those shown in subsection 2.3.1.

Secondly, the values of the trimer angles of the low-energy trimers are greatly affected by the second-order interactions. Two of the 10 lowest-energy conformations have C_2 symmetry[13]. Thus, in the framework of the RIS calculation, there are $8 \times 4 + 2 \times 2 = 36$ rotational isomeric states for the five torsion angles of one trimer unit. Interestingly, none of the 10 low-energy trimers contains two type-II pairs. Since

dimer pairs	trimer angle(°)	E′(trimer) (Kcal/mol)
(D1,D5),(D5,D2)	-64	0.0 (ε_1)
(D3,D6),(D6,D4)	64	0.0
(D1,D6),(D6,D2)	91	0.1 (ε_2)
(D3,D5),(D5,D4)	-91	0.1
(D1,D1),(D2,D2)	-73	1.5 (ε_3)
(D4,D4),(D3,D3)	73	1.5
(D1,D3),(D4,D2)	-75	1.5 (ε_4)
(D3,D1),(D2,D4)	75	1.5
(D1,D1),(D2,D2)	101	1.8 (ε_5)
(D4,D4),(D3,D3)	-101	1.8
(D1,D2)	-62	1.8 (ε_6)
(D3,D4)	62	1.8
(D2,D5),(D5,D1)	-80	1.9 (ε_7)
(D4,D6),(D6,D3)	80	1.9
(D1,D4),(D3,D2)	-83	2.3 (ε_8)
(D3,D2),(D1,D4)	83	2.3
(D2,D1)	88	2.8 (ε_9)
(D4,D3)	-88	2.8
(D2,D3),(D4,D1)	90	3.1 (ε_{10})
(D4,D1),(D2,D3)	-90	3.1

Table 2.3: Low energy conformations of a trimer. D1 to D6 respectively denote the dimer pairs $(20°, 145°)$, $(145°, 20°)$, $(-20°, -145°)$, $(-145°, -20°)$, $(110°, 110°)$ and $(-110°, -110°)$. Parameters from O'Hare et al.[13], where two dimer energies are subtracted from the trimer energy to get the second-order interaction energy E′(trimer). The ε_i denotations are used in Appendix A.

the energy difference between the lowest-energy trimer and the tenth-lowest-energy trimer is 2.1Kcal/mol $\approx$ 3kT, it is reasonable to only choose these 36 rotational isomeric states in the RIS ensemble (Table 2.3). Based on such construction, there are 20 rotational isomeric states in total for the trimer angles.

2.3.3 Configurational Energy of An Ideal PFDMS Chain

The configuration energy of an ideal chain only depends on the short-range interactions [10, 15]. Based on the RIS ensemble constructed for PFDMS, which is dictated by the first-order and second-order interactions, the statistical weight matrices (U-matrices) used in this work have large dimensions. They are alternating 6×6, 20×6 and 6×20 matrices (See details in Appendix A).

To proceed, we write the configurational energy of an ideal PFDMS chain $Fc[Fe(C_5H_4)_2SiMe_2]_nH$ as

$$\begin{aligned} E(chain) &= \sum_{i=1}^{n} E(dimer\ i) + \sum_{j=1}^{n-1} E'(trimer\ j) \\ &= \sum_{i=1}^{n} E(\phi_i, \psi_i) + \sum_{j=1}^{n-1} E'(\phi_j, \psi_j, \chi_j, \phi_{j+1}, \psi_{j+1}) \end{aligned} \tag{2.2}$$

One essential idea of the RIS model is that the statistical integral over all torsion angles can be approximated by the sum of finite number of isomeric states, which correspond to the potential minima[10]. The probability assigned to each isomeric state, $\exp(-E/kT)$, needs to be explained here. Strictly speaking, the E should be regarded as free energy. If the shapes of the potential minima in the plot of potential energy as a function of the torsion angles are similar, replacing the value of E with the energy at the minima does not affect the final statistics[10]. For the PFDMS chain, this condition needs to be carefully examined. As shown in Figure 2.5, the shapes of the potential minima at the type-I pair and the type-II pair differ. The former is wider, or, the local entropy around the type-I pair is larger, enhancing its probability. In order to examine this effect, we use g_1 and g_2 ($g_1 > g_2$) to denote the

effective degeneracies of energy for the type-I pair and the type-II pair, respectively. Then, the probabilities assigned to the two type of rotational isomeric state are equal to $g_1 \exp(-E_1/kT)$ and $g_2 \exp(-E_2/kT)$, where E_1 and E_2 denote the values of the energy minima at the type-I pair and the type-II pair, respectively. Below, we introduce $\Delta E = kT \ln(g_1/g_2)$. Since the final statistics only depends on the relative probability of the two types of rotational isomeric states, we can still use the formula $\exp(-E/kT)$ to compute probability by assigning the following energy values to each rotational isomeric state

$$E(dimer) = \begin{cases} 0 & \text{type-I pair} \\ 1.0 \text{ Kcal/mol} + \Delta E & \text{type-II pair} \end{cases}$$

$$E'(trimer) = \begin{cases} \text{10 types of energies for 20 types of} \\ \text{trimer angles and 36 types of} \\ \text{trimer conformations (Table 2.3)} \end{cases}$$

ΔE actually determines the relative probability of type-I pairs and type-II pairs in the chain, thus, its influences to the configurational properties can be examined by observing the calculation results in a range of ΔE, which is performed in next section.

2.4 Results

Once the RIS model and its parameters are defined, several physical quantities can be calculated. In what follows, the following parameters are considered:

1. The root-mean-square of the distance between two terminal Cp centroids, $r_0 = \langle r^2 \rangle_0^{1/2}$. Details of computing r_0 are given in Appendix A.

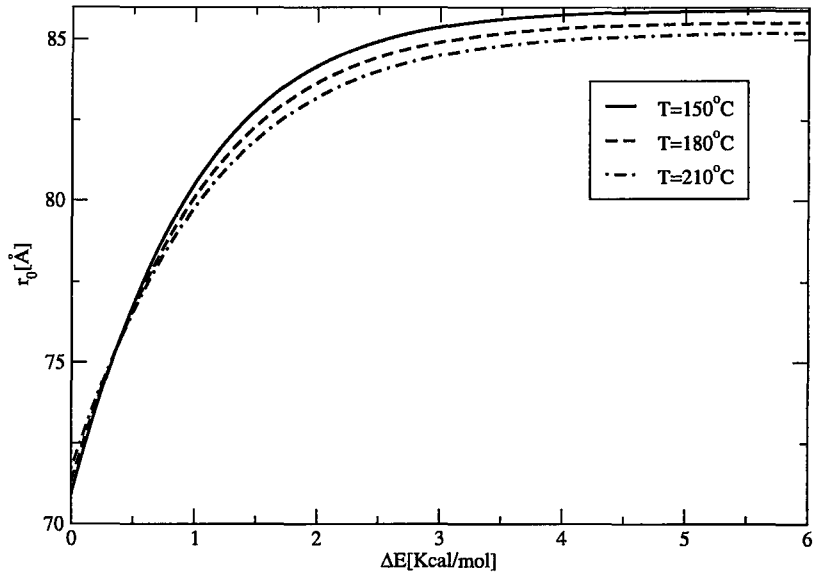

Figure 2.6: Root-mean-square of the end-to-end distance of a n=100 ideal PFDMS chain as the function of ΔE at temperatures 150°C, 180°C and 210°C.

2. The characteristic ratio [10], defined by $C_n = \langle r^2 \rangle_0 / N\bar{l}^2$, where N is the number of bonds in the backbone of PFDMS and $\bar{l}^2$ is the mean-square bond length. The backbone of the PFDMS chain is $\mathrm{C-Fe-[C-Si-C-Fe]_n-C}$, thus, $N = 4n+2$. The asymptotic limit of $C_n(n(N) \to \infty)$ is denoted as C_∞. From bond lengths shown in Table 2.1, it is determined that $\bar{l}^2 = 3.79$ Å^2.

3. The root-mean-square distance of all iron atoms in an ideal PFDMS chain from their center of gravity, i.e., the radius of gyration, $R_{g0} = \langle R_g^2 \rangle_0^{1/2}$. Because of the chemical and physical properties of the iron atoms, this definition is more appropriate to experimental researchers. The formulas are given in Appendix B.

4. The temperature coefficient $d \ln \langle r^2 \rangle_0 / dT$[10].

The glass transition temperature T_g of PFDMS is 33 °C and the melting temperature T_m is 122 $\sim$ 145 °C[2]. Since the RIS model is only valid for the chains in melts

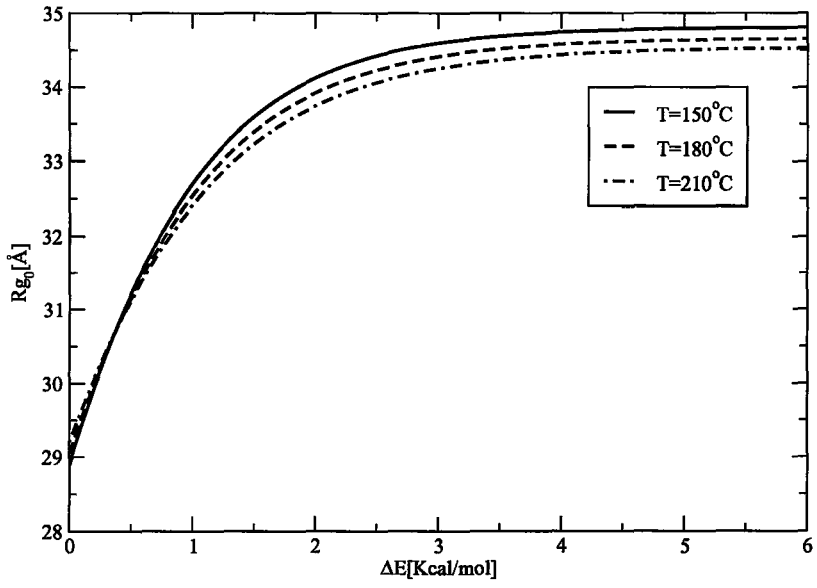

Figure 2.7: Root-mean-square of the radius of gyration of all iron atoms for a n=100 ideal PFDMS chain as the function of ΔE at temperatures 150°C, 180°C and 210°C.

or Θ-solvents, our calculations were carried out at 150 °C, 180 °C and 210 °C (above T_g and T_m). The effect of ΔE is examined. The results are summarized in Figure 2.6-2.12.

(1) For given n and T, both r_0 and R_{g0} increase with ΔE (Figure 2.6 and 2.7). The most sensitive range is 0-2 Kcal/mol. On the other hand, the temperature dependence of the unperturbed dimensions is quite weak. For a fixed ΔE, the C_n values are very close at the three different temperatures. In what follows, we use the calculation results at T=180°C to estimate C_n and C_∞.

(2) C_n increases with n and quickly converges to an asymptotic limit C_∞ (see Figure 2.8). It is found that C_∞ is bounded in the range 3.4-4.8 and increases with ΔE. To better show the relationship between C_n and C_∞, we use the "C_n vs $1/n$" diagram (see Figure 2.9). It is found that when $n \gtrsim 10$, a linear formula

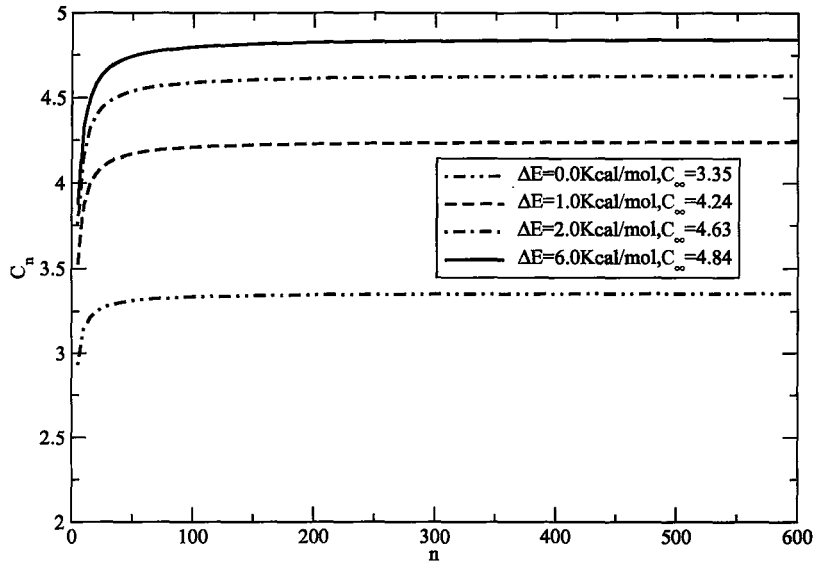

Figure 2.8: The characteristic ratios of PFDMS at different ΔE (T = 180°C). The asymptotic limit C_∞ are shown in the box.

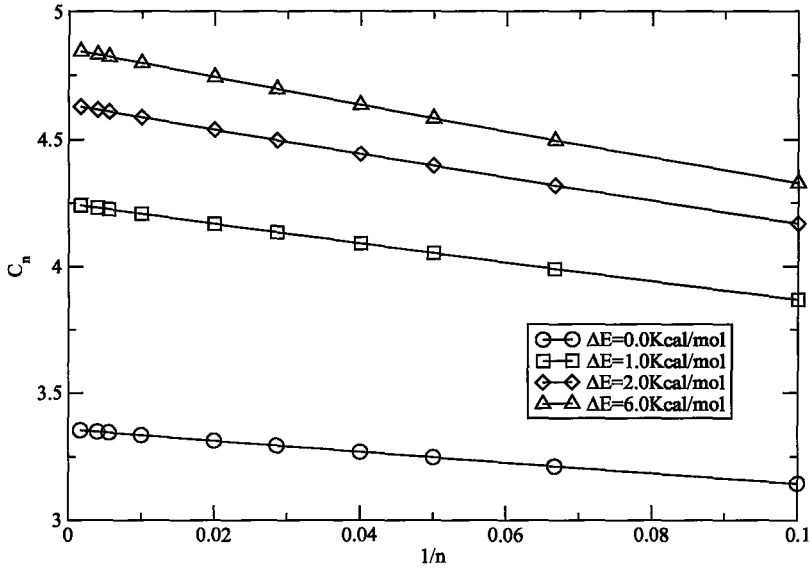

Figure 2.9: C_n vs $1/n$ (T = 180°C). The ten samples are calculated at (from right to left) n=10, 15, 20, 25, 35, 50, 100, 180, 250 and 600. $C_\infty^{-1}[dC_n/d(1/n)]_{1/n=0}$ are equal to -0.64, -0.90, -1.02 and -1.09 respectively for the four ΔE values from 0.0 to 6.0 Kcal/mol.

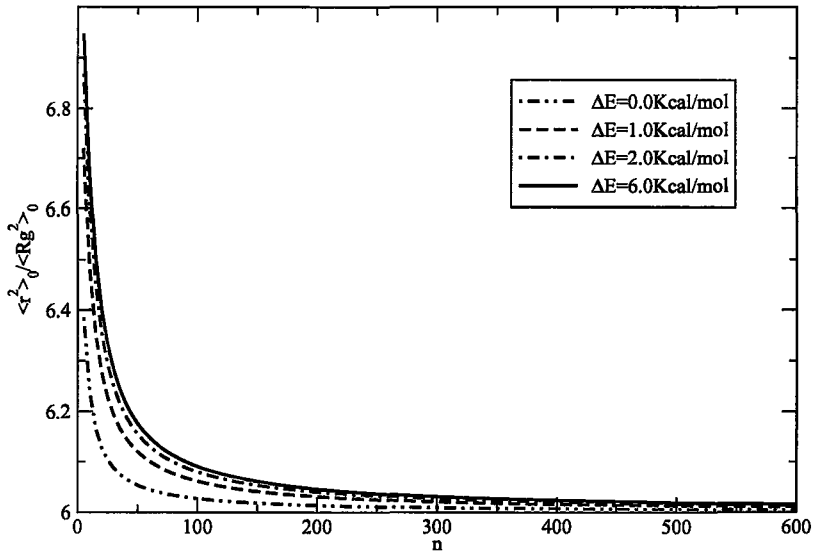

Figure 2.10: $\langle r^2\rangle_0 / \langle R_g^2\rangle_0$ (T = 180°C). The approach of $\langle r^2\rangle_0 / \langle R_g^2\rangle_0$ to its limiting value of 6 is from above.

$C_\infty + (1/n) \times [dC_n/d(1/n)]_{1/n=0}$ is an accurate approximation of C_n. Mattice et al. have discussed this type of relationship in depth[16], where polymers with similar C_∞ values but obviously different slopes $[dC_n/d(1/n)]_{1/n=0}$ are shown. From our calculations, the value of $C_\infty^{-1}[dC_n/d(1/n)]_{1/n=0}$ for PFDMS is around -1.0 (Figure 2.9), whose magnitude is much smaller than the counterpart of the three common polymers polyethylene(PE), polyisobutylene(PIB) and polydimethylsioxane(PDMS) considered in ref 16. The relatively low C_∞ and fast convergence of C_n to C_∞ with increasing n show that PFDMS is of high static flexibility. Therefore, relatively more compact random-coil conformations of PFDMS chains are expected in the melts.

(3) The general relationship $\langle r^2\rangle_0 / \langle R_g^2\rangle_0 \to 6$ for $n \to \infty$ for flexible ideal polymers is confirmed in Figure 2.10. The approach of $\langle r^2\rangle_0 / \langle R_g^2\rangle_0$ to 6 is from above. As shown in Figure 2.11, When $n \gtrsim 25$, a linear formula $6.0 + (1/n) \times [d(\langle r^2\rangle_0 / \langle R_g^2\rangle_0)/d(1/n)]_{1/n=0}$ is an accurate approximation of $\langle r^2\rangle_0 / \langle R_g^2\rangle_0$. The

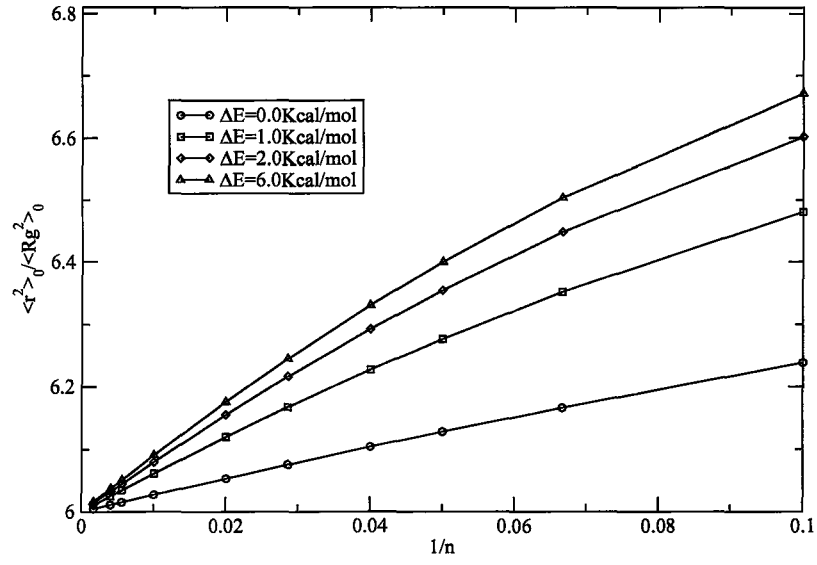

Figure 2.11: $\langle r^2\rangle_0 / \langle R_g^2\rangle_0$ vs $1/n$ (T = 180°C). The ten samples are calculated at (from right to left) n=10, 15, 20, 25, 35, 50, 100, 180, 250 and 600. $[d(\langle r^2\rangle_0 / \langle R_g^2\rangle_0)/d(1/n)]_{1/n=0}$ are equal to 2.60, 5.68, 7.30 and 8.26 respectively for the four ΔE values from 0.0 to 6.0 Kcal/mol.

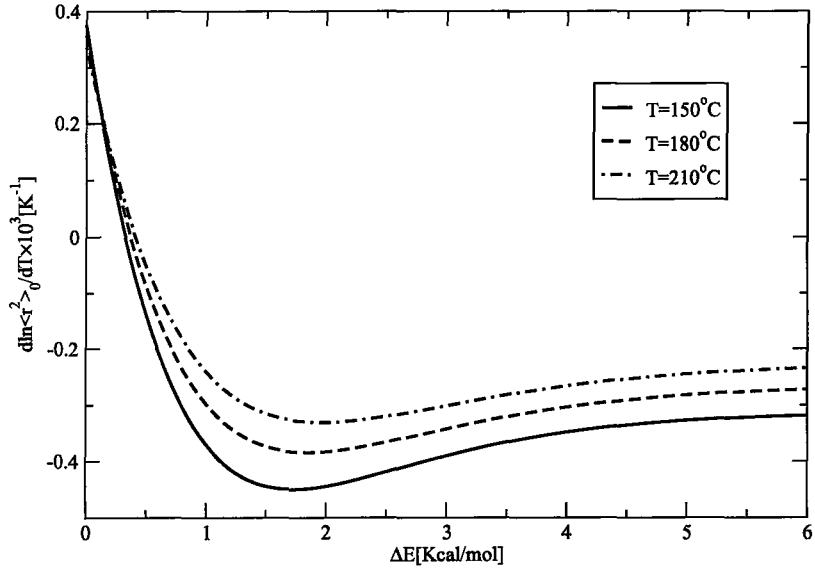

Figure 2.12: Temperature coefficient of n=100 ideal PFDMS chain as the function of ΔE at temperatures 150°C, 180°C and 210°C.

slope $[d(\langle r^2\rangle_0 / \langle R_g^2\rangle_0)/d(1/n)]_{1/n=0}$ increases with ΔE.

(4) The sign of the temperature coefficient changes from + to - with increasing ΔE. The dividing line is around $\Delta E = 0.5$ Kcal/mol (Figure 2.12).

In the RIS calculation, the probability that one dimer pair is a type-I(II) pair increases(decreases) with ΔE. Thus, based on the fact that the conformation of one dimer unit containing a type-II pair is more compact than the conformation of one dimer unit containing a type-I pair (the Fe-Fe distance is 5.61 Å for one dimer unit containing a type-II pair and 5.95 Å for one dimer unit containing a type-I pair[13]), we would expect the unperturbed dimensions of one PFDMS chain increase with ΔE. The results shown above are consistent with this expectation.

For the illustative curves shown in Figure 2.6-2.12, values of ΔE in a big range (0-6 Kcal/mol) are considered. However, based on the plot of energy as a function of the two torsion angles (dimer pair) of one dimer shown in Figure 2.5, we estimate the real value of ΔE for PFDMS is in the range of 0.4-2.0 Kcal/mol. This leads to our estimation $C_\infty = 4.2 \pm 0.4$ for PFDMS.

Finally, we calculate the Kuhn length l_K of an ideal PFDMS chain based on the calculated C_∞. For large n, the relation between $\langle r^2\rangle_0$ and n, a and l_K is

$$\langle r^2\rangle_0 = nal_K \tag{2.3}$$

where a is the monomer size. Because the effective volume of one monomer is a^3, we can estimate a using the relation

$$a = \left(\frac{M_0}{\rho_b N_{AV}}\right)^{1/3} \tag{2.4}$$

where $M_0 = 242$ g/mol is the molar mass of a PFDMS monomer, $\rho_b \approx 1.26$ g/mL is the density of bulk PFDMS[17]. Using these parameters we obtain $a = 6.8$ Å. For large n, we also have

$$\langle r^2 \rangle_0 = 4nC_\infty \bar{l}^2 \tag{2.5}$$

therefore, l_K and C_∞ satisfy the relation

$$l_K = 4C_\infty \bar{l}^2 / a \tag{2.6}$$

This gives $l_K = 9.4 \pm 0.8$ Å.

To the best of our knowledge, the Kuhn length of an ideal PFDMS chain has not been addressed either by experiments or by theoretical calculations. We hope the results obtained in this work are helpful to the current research on polyferrocenylsilanes.

2.5 Discussions

In conclusion, we have examined the configurational statistics of an ideal PFDMS chain using the RIS model in this chapter. The RIS chain and ensemble are constructed based on the geometrical and energetic features of PFDMS. Calculated configurational quantities include $\langle r^2 \rangle_0$, $\langle R_g^2 \rangle_0$, $C_n(C_\infty)$ and $d \ln \langle r^2 \rangle_0 / dT$. The results show that an ideal PFDMS chain is of high static flexibility. The previously unknown Kuhn length of PFDMS is also obtained based on the calculated C_∞.

According to the ESFF calculation carried out by O'Hare et al., replacement of the methyl groups in the organosilane unit of PFDMS with longer alkyl chains has

very little effect on the relative orientation of the ferrocene units[13]. This is because the conformational energies are almost exclusively determined by the non-bonding electrostatic interactions between the positively charged iron atoms and negatively charged Cp rings in the ferrocene units, while the energetic contribution from the organosilane units containing alkyl side groups is much smaller. Thus, the configurational properties of PFDMS should be close to the configutational properties of the polyferrocenylsilanes with longer alkyl chains in the organosilane units.

On the other hand, low-energy conformations of polyferrocenylsilanes with other types of side groups might be different from the low-energy conformations of PFDMS. Using the RIS model to investigate the configurational properties of such types of PFS requires constructing new RIS ensembles rather than what used in this work.

Chapter 3

Self-Assembly of PFS-b-PDMS in Alkane Solutions

3.1 Introduction

Polyferrocene block copolymers are expected to self-assemble to form micellar aggregates in selective solvents for one of the blocks. This would allow the generation of unique supermolecular organometallic polymer assemblies[2]. In recent years, Manners et al. have shown that diblock copolymers consisting of a poly(ferrocenyldimethylsilane) block connected to a poly(dimethylsiloxane) block (PFS-b-PDMS) self-assemble to from interesting and unusual cylindrical structures in alkane solvents with large PDMS/PFS block ratios[6, 7, 8, 9]. Simple alkanes are modest to poor solvents for PDMS but nonsolvents for PFS[18]. Although we would expect the insolubility of PFS drives a self-assembly process, the formation of cylindrical structures is surprising since most asymmetric diblock copolymers in solvents selective for the longer

block form spherical micelles.

The driving force for the formation of cylindrical micelles was partially clarified by Manners et al.[6, 9]. For all experiments in which cylindrical structures were observed, the temperatures were below the melting temperature T_m of PFS (ca. 120-145 °C). Therefore, the crystallization of the PFS blocks was taken as the main factor which rejects the formation of spherical micelles. Two supplemental experiments supported this conclusion. Either increasing the temperature above T_m of PFS or replacing the crystalline PFS blocks by amorphous polyferrocenylmethylphenylsilane or polyferrocenylmethylethylsilane blocks, spherical micelles were formed as expected[6].

If the insoluble block is amorphous rather than crystalline, the copolymer is referred to as a "coil-coil" diblock copolymer. To date, most theoretical studies of the self-assembly of diblock copolymers in solutions have discussed this class of polymers. In contrast, we have much poorer theoretical understanding of the self-assembly of crystalline-coil diblock copolymers in solutions. In this chapter, we present our theoretical model to investigate the self-assembly of PFS-b-PDMS in alkanes below T_m of PFS. There are two-fold values of this work. On one hand, PFS-b-PDMS copolymers can be taken as crystalline-coil model systems. The experimental observations of Manners et al. indicate that apart from the wellknown lamellar micelles, rodlike or tubular micelles also could be thermodynamically stable in crystalline-coil systems. Thus, studies of these three types of micelles in depth should enable a better understanding of the fundamental physics underlying the self-assembly of crystalline-coil diblock copolymers in solutions. On the other hand, a better understanding of the interplay of factors that affect the aggregate properties of PFS-b-PDMS copolymers

is desirable for potential applications which take advantage of self-assembly of polyferrocene block copolymers[2].

The subsequent contents of this chapter are organized as follows: In section 3.2, we propose the theoretical model, in which three types of aggregates — lamellar, rodlike and tubular micelles are considered, in accordance with the experimental observations of Manners et al. For each morphology, we show the assumed microscopic structure and derive the formulas of the free energy per copolymer chain which dictate the phase behaviours. Main results are given in section 3.3, where three types of phase diagrams are predicted. Finally in section 3.4, we discuss the possible improvement of the model and analyze the current challenges of studying PFS-b-PDMS self-assembly in alkane solvents for both theories and experiments.

3.2 Model

In previous literatures, several features of the self-assembly of crystalline-coil copolymers in selective solvents for the coil blocks have been suggested. First, unlike the homopolymer crystallization, which is a kinetic process (e.g., the number of folds per chain depends on the crystal growth rate[19]), the self-assembled structure of the crystalline-coil copolymers is believed to be thermodynamically determined, i.e., minimal free energy dictates the micellar morphology[20]. Secondly, crystal packing forces play a dominant role in determining the structure of the crystalline core. The most common self-assembled structure expected and experimentally verified is a plate (lamella), with the corona blocks protruding from both faces. To date, most theoret-

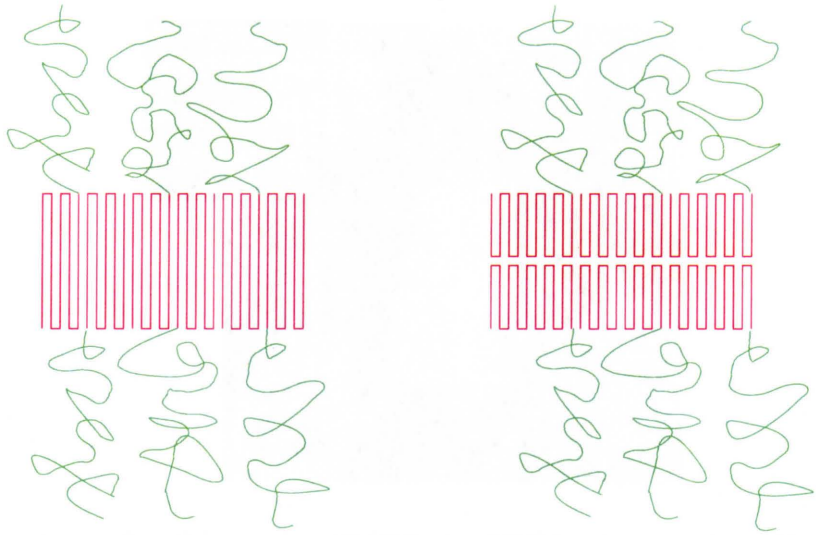

Figure 3.1: Schematic of two types of lamellar morphologies: the crystalline core is a monolayer structure (left) or a bilayer structure (right). In this example, the thickness of the core is identical for the two types of lamellar micelles.

ical works of the self-assembly of crystalline-coil copolymers in selective solvents for the coil blocks focused on this morphology. It is clear that the thickness of the plate is balanced by two opposite trends: the system can minimize the repulsion between adjacent coils of the corona block by increasing the number of folds in the core, leading to a thinner plate, or it can minimize the corona/core interface free energy by decreasing the number of folds in the core, leading to a thicker plate. The fact that the crystalline core of the lamellar micelle is a monolayer structure rather than bilayer structure has also been theoretically explained[21]. Consider two lamellar micelles, one has a monolayer crystalline core and the other has a a bilayer crystalline core. The core thickness of the two micelles are identical (Figure 3.1), therefore, the number of folds per chain for the bilayer one is two times of the number of folds per chain for the monolayer one. Because the interface area per chain is identical for the two micelles, the corona free energy and the corona/core interface free energy would also

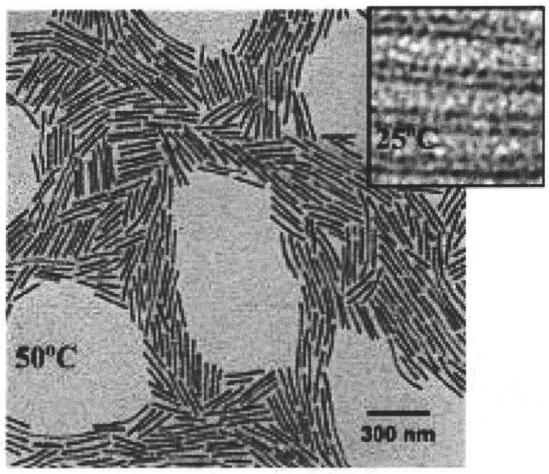

Figure 3.2: TEM micrograph of PFS_{40}-b-$PDMS_{480}$ assemblies formed in n-decane at 50°C (short dense rods) and 25°C (nanotubes). The picture is taken from Manners et al.[9].

be identical. However, more number of folds would cost more folding energy. This justifies that the total free energy of the monolayer one is lower than the bilayer one. Thirdly, non-lamellar structures are possible. Vilgis and Halperin have discussed this possibility by a scaling analysis[20]. They postulated the so-called starlike micelles formed from crystalline-coil copolymers with a core in the form of a rectangular solid and showed that with long enough corona blocks, such micelles would be thermodynamically more preferred than lamellar micelles.

The experimental observations in the PFS-b-PDMS/alkane system by Manners et al. verified the existence of non-lamellar structures, although the observed cylindrical micelles (Figure 3.2) were not expected in the original work of Vilgis and Halperin (VH). However, as shown below, these morphologies are consistent with VH's viewpoint that long enough corona blocks would lead to non-lamellar structures. Since two types of non-lamellar (rodlike and tubular) micelles were observed in the PFS-

b-PDMS/alkane system, in what follows, we focus the theory and computation on three types of morphologies: lamellar, rodlike and tubular morphologies.

When the copolymer concentration is larger than a critical value Φ^*, which is called the critical micelle concentration (CMC), an aggregation process occurs. In the disorder state, the unfavorable interactions between the solvophobic blocks and the solvents would cost much energy. Thus, even at very small polymer concentration, the free energy released by forming micelles encapsulating the solvophobic blocks would dominate the loss of the translational entropy. This is why CMC is usually very low (typically at volume fraction of $10^{-4} - 10^{-8}$[22]). There is another critical concentration Φ^{**}, above which the effect of the interactions between aggregates become important and can not be ignored. In our theory, we assume the copolymer concentration Φ falls within the range $\Phi^* < \Phi \ll \Phi^{**}$. The interactions between micelles are therefore ignored.

3.2.1 Morphological Geometry

We follow the original ideas of VH[20]. The crystalline blocks are assumed to undergo chain-fold crystallization and the crystallinity is assumed to be 100%. It is also assumed that the chains fold back at adjacent sites (adjacent reentry) and the solvents are excluded from the crystalline core. Therefore, the crystalline block can be viewed as N_f (number of folds) close-packed rod-like chains.

In addition, PDMS and PFS are generally incompatible. For the block lengths interested in the current work, the strong segregation regime condition $\chi N \gg 10$[23]

is satisfied. In our model, we ignore the thickness of the corona/core interface and assume the junction points between two blocks are uniformly distributed on a planar (for lamellar and rodlike micelles) or cylindrical (for tubular micelles) surface. For a microscopic theory, the thickness of the interface is important in determining the interface free energy. However, in the current work, we assume that the interface free energy is characterized by two phenomenological parameters (see details in subsection 3.2.2).

We use N_A and N_B to denote the degrees of polymerization of the PDMS(coil) strand and PFS(crystalline) strand, respectively. The monomer size a_A and the Kuhn length l_{K_A} of PDMS blocks are determined to be 5.0 $\AA$ and 6.9 $\AA$ based on the same computational method described in section 2.4. Other PDMS parameters are the density of bulk 0.97 g/mL[24], the C_∞ value 6.43[10], the Si-O bond length 1.64 $\AA$[10] and the molar mass 74 g/mol. Moreover, we model the segment of the crystalline PFS blocks as a $a_B \times a_B \times l_B$ square cuboid. Because a strong peak at ca. 6.4 $\AA$ was observed in the wide-angle X-ray scattering pattern of crystalline PFS[6], we approximate a_B as 6.4 $\AA$. We also assume the crystalline and amorphous PFS have the same density of bulk, which leads to a approximate value of 7.7 $\AA$ for l_B.

Lamella

The schematic of the lamellar morphology is shown in Figure 3.3. We assume that the PDMS volume fraction c in the coronas is a constant. For the current system, where alkanes are modest to poor solvents for PDMS, this type of mean-field treatment is acceptable. The thickness of the crystalline PFS core d and the height

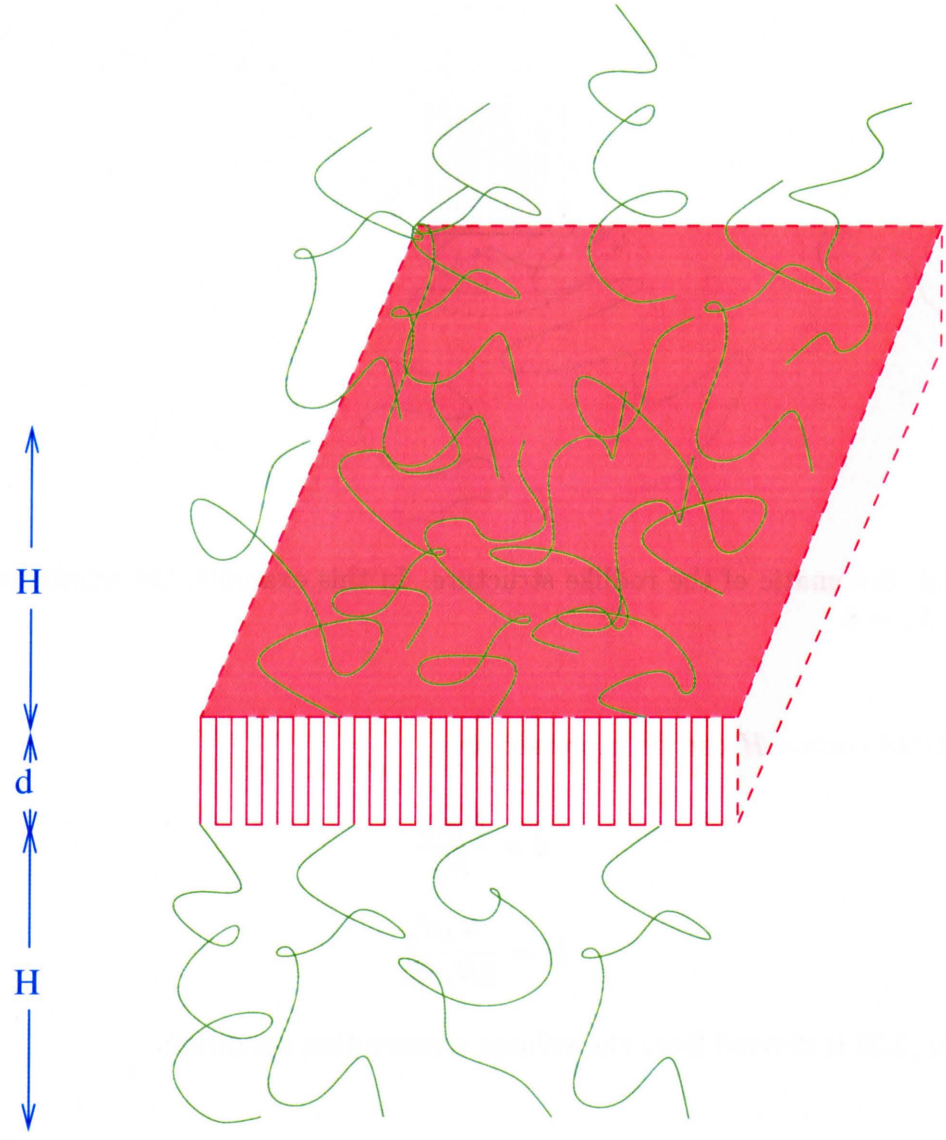

Figure 3.3: Schematic of the lamellar structure. In this example, the number of folds is $N_f = 5$.

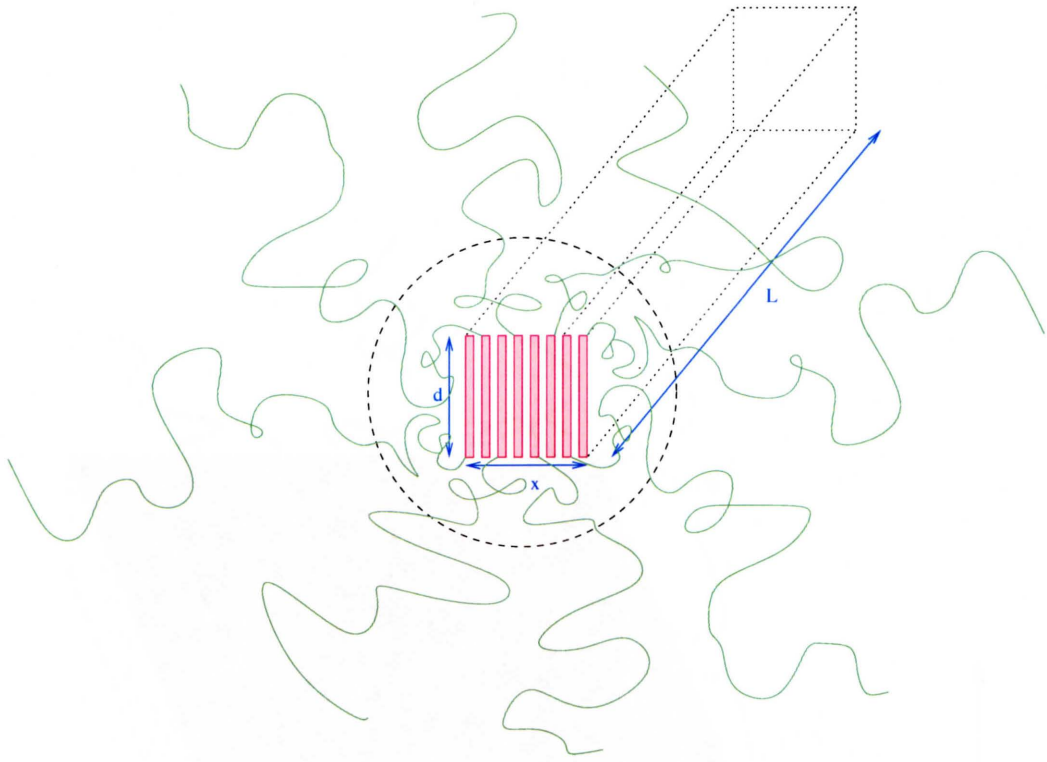

Figure 3.4: Schematic of the rodlike structure. In this example, the number of "ribbons" is $N_r = 8$.

of the PDMS corona H can be expressed as:

$$d = \frac{N_B l_B}{N_f} \tag{3.1}$$

$$H = \frac{N_A a_A^3}{2 N_f a_B^2 c} \tag{3.2}$$

where Eq.(3.2) is derived from the volume conservation condition.

Rod

The assumed molecular geometry of the rodlike morphology observed in the PDMS-b-PFS/alkane system is shown in Figure 3.4, where the crystalline orientation of the PFS blocks is perpendicular to the long axis of the rodlike micelle. The PFS core can be viewed as an assembly of N_r rigid "ribbons". The thickness of a "ribbon" is a_B.

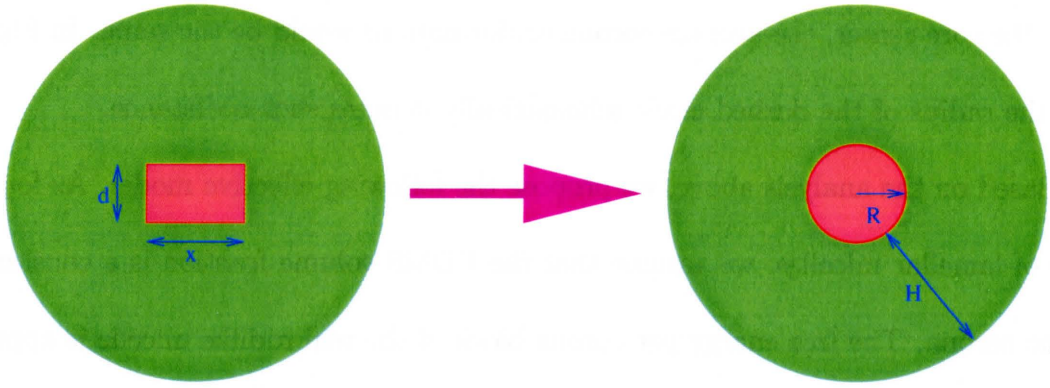

Figure 3.5: Proposed effective morphology (right) for computing the approximate corona free energy. The real rodlike morphology is shown left.

Note the assumed chain-fold crystallization does not require that all the N_f folded blocks of one chain are in the same "ribbon". Based on these descriptions, We can determine $x = N_r a_B$, $d = N_B l_B / N_f$ and the aspect ratio $\eta = d/x = N_B l_B / N_f N_r a_B$ for the PFS core which is in the shape of a long cuboid.

We now turn to the PDMS corona of this rodlike morphology. For the most common cylindrical micelles, typically formed in the coil-coil systems, the solvophobic core is in the form of a cylinder. Therefore, the grafted ends of the corona blocks are uniformly distributed on the cylindrical core surface. In contrast, as shown in Figure 3.4, the gafted ends of the corona blocks of the rodlike micelles are only distributed on two opposite surfaces of the core cuboid. However, since we are only interested in long corona blocks, we can expect the outer boundary of the corona is approximately a cylindrical surface for both cases. As illustrated in Figure 3.5, the outer boundaries of the corona's cross sections in both cases are circular. Although the local conformations of the corona blocks near the core are different due to the different grafted surface geometry of these two cases, beyond some critical distance

from the core center, the average corona conformations would be the same. In Figure 3.4, the radius of the dashed circle schematically denotes such a distance.

Based on the analysis above, we propose the following effective model. As for the case of lamellar micelles, we assume that the PDMS volume fraction is a constant c in the corona. The free energy per corona block of the real rodlike micelle is approximated by the free energy per corona block of the effective morphology, in which the core is of a cylindrical structure and of the same volume as the core of the real rodlike micelle (Figure 3.5). The geometrical parameters of this effective morphology can be determined using volume conservation conditions:

$$R = (dx/\pi)^{1/2} = \pi^{-1/2} N_B^{1/2} N_f^{-1/2} N_r^{1/2} l_B^{1/2} a_B^{1/2} \tag{3.3}$$

$$\frac{H}{R} = \left(\frac{N_A a_A^3}{N_B a_B^2 l_B c} + 1 \right)^{1/2} - 1 \tag{3.4}$$

In addition, the interface area per chain α in this effective morphology is

$$\alpha = 2\pi^{1/2} N_B^{1/2} N_f^{1/2} N_r^{-1/2} a_B^{3/2} l_B^{1/2} \tag{3.5}$$

This treatment enables the computation of the conformational free energy of the PDMS(coil) blocks in a unified framework for lamellar, rodlike and tubular micelles (see details in Appendix C). In the current work, we introduce two phenomenological parameters γ_g and γ_n to denote the surface free energy per unit area of grafted surfaces and non-grafted surfaces in the real rodlike morphology. The error caused by ignoring the conformational difference of the corona block segments near the core is expected to be partially reduced by including the energy cost of the irregular local conformations near the non-grafted surfaces in γ_n.

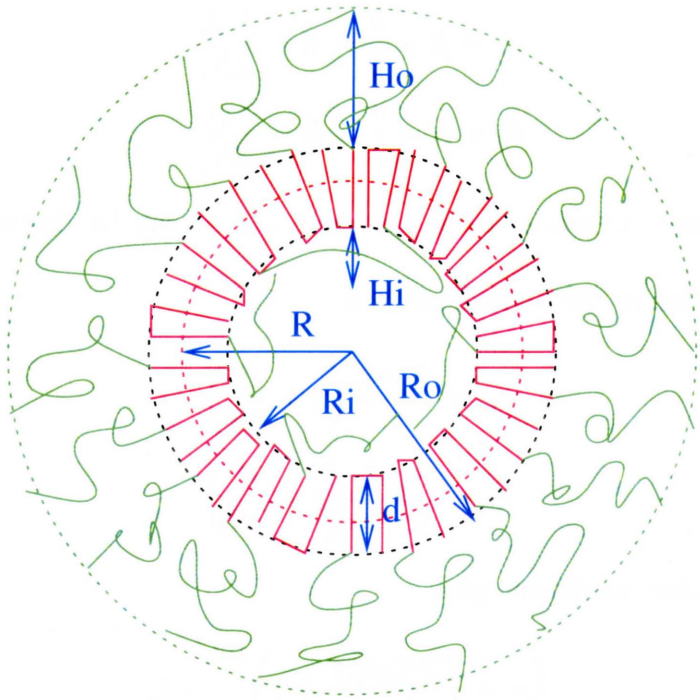

Figure 3.6: Schematic of the cross section of the tubular structure. In this example, the number of folds is $N_f = 2$.

Tube

The tubular morphology is unusual. As shown in Figure 3.6, we model the crystalline core as a cylindrical shell with PDMS blocks protruding from both outer and inner surfaces. Different from lamellar and rodlike micelles, this core geometry would lead to extra deformational energy. We let τ denote the number fraction of the PDMS in the outer corona. We also assume that the PDMS volume fractions in the outer and inner coronas are constants, denoted by c_o and c_i, respectively. We take the radius of the cylindrical neutral surface R as a thermodynamical variable. Then the thickness, outer and inner radiuses of the crystalline shell satisfy:

$$d = \frac{N_B l_B}{N_f} \tag{3.6}$$

$$R_o = R + \frac{d}{2} = R + \frac{N_B l_B}{2N_f} \tag{3.7}$$

$$R_i = R - \frac{d}{2} = R - \frac{N_B l_B}{2N_f} \tag{3.8}$$

The outer and inner interface areas per chain α_o, α_i can be derived based on the zero-strain condition of the neutral surface:

$$\alpha_o = \frac{N_f a_B^2}{\tau}\left(1 + \frac{d}{2R}\right) \tag{3.9}$$

$$\alpha_i = \frac{N_f a_B^2}{1-\tau}\left(1 - \frac{d}{2R}\right) \tag{3.10}$$

Volume conservation conditions give:

$$\frac{H_o}{R_o} = \left(\frac{2N_A a_A^3 \tau}{R_o \alpha_o c_o} + 1\right)^{1/2} - 1 \tag{3.11}$$

$$\frac{H_i}{R_i} = 1 - \left[1 - \frac{2N_A a_A^3 (1-\tau)}{R_i \alpha_i c_i}\right]^{1/2} \tag{3.12}$$

3.2.2 Free Energy Formulas

In general, we can express the free energy as $F = F_{corona} + F_{core} + F_{interface}$. The computation of the conformational free energy of corona blocks is summarized in Appendix C. For other terms of the free energy formulas, the main theoretical assumptions include:

(1) The energy cost of one fold is E_f[21]. The folding energy per chain is $N_f E_f$.

(2) We let $x_1 = (E_f + 2\gamma_g a_B^2)/kT$, $x_2 = 2\gamma_n a_B^2/kT$ and by first-order approximation, take them as dimensionless constants for a specific crystalline-coil copolymer/solvent system.

(3) The deformational energy of the crystalline shell in the tubular morphology is estimated by a simple curvature expansion theory[22]. For the crystalline

shell discussed, the zero-curvature structure, i.e., planar structure, corresponds to the deformational energy minimum. Therefore, by incorporating the curvatures of the cylindrical and spherical shells, the deformational energy per unit neutral surface area can be expressed as:

$$F_d = \begin{cases} 0 & \text{Planar shell} \\ \frac{1}{8}K_d d^2/R^2 & \text{Cylindrical shell} \\ \frac{1}{2}K_d d^2/R^2 & \text{Spherical shell} \end{cases}$$

where K_d is the elastic modulus whose magnitude originates from the molecular interactions that constitute the shell. We let $x_3 = K_d a_B^2/kT$ and, by first-order approximation, take it as a dimensionless constant for a specific crystalline-coil copolymer/solvent system.

(4) For a corona with block volume fraction c, we use mean-field theory to estimate the translational entropy of the solvents and the effective interaction energy between the coil segments and solvent molecules, which lead to:

$$F_{corona}/kT = f_c + N_A(1-c)\left[\frac{1}{c}\ln(1-c) + \chi_{AS}\right] \tag{3.13}$$

The formulas of f_c are derived in Appendix C. χ_{AS} is the Flory-Huggins parameter quantifying the coil-solvent interaction. For PDMS coils and alkane solvents, χ_{AS} decreases with temperature, i.e., higher temperature leads to better solubility. We have also assumed the size of the solvent molecule is comparable with the size of the coil segment.

Based on the model described above, we determine the formulas of the free energy per copolymer chain as follows:

Lamella

$$F/kT = N_f x_1 + \frac{\pi^2 N_A a_A^5}{32 N_f^2 l_{K_A} a_B^4 c^2} + N_A(1-c)\left[\frac{1}{c}\ln(1-c) + \chi_{AS}\right] \tag{3.14}$$

Rod

$$F/kT = N_f x_1 + \frac{N_B l_B x_2}{N_r a_B} + N_A(1-c)\left[\frac{1}{c}\ln(1-c) + \chi_{AS}\right] + \frac{\pi N_B^2 N_r l_B^2 a_B^3 c}{16 N_A^2 N_f l_{K_A} a_A^4}\left[\left(\frac{N_A a_A^3}{N_B a_B^2 l_B c} + 1\right)^{1/2} - 1\right]^3 \left[3\left(\frac{N_A a_A^3}{N_B a_B^2 l_B c} + 1\right)^{1/2} + 1\right] \tag{3.15}$$

Tube

$$\begin{aligned} F/kT = {} & N_f x_1 + \frac{N_B^2 l_B^2 x_3}{8 N_f R^2} + N_A(1-c_o)\tau\left[\frac{1}{c_o}\ln(1-c_o) + \chi_{AS}\right] + \\ & N_A(1-c_i)(1-\tau)\left[\frac{1}{c_i}\ln(1-c_i) + \chi_{AS}\right] + \\ & \frac{\pi^2 N_f a_B^2 R_o^3 c_o}{8 N_A^2 l_{K_A} a_A^4 \tau}\left(\frac{H_o}{R_o}\right)^3\left[1 + \frac{3}{4}\left(\frac{H_o}{R_o}\right)\right]\left(1 + \frac{d}{2R}\right) + \\ & \frac{\pi^2 N_f a_B^2 R_i^3 c_i}{8 N_A^2 l_{K_A} a_A^4 (1-\tau)}\left(\frac{H_i}{R_i}\right)^3\left[1 + \frac{3}{4}\left(\frac{H_i}{R_i}\right)\right]\left(1 - \frac{d}{2R}\right) \end{aligned} \tag{3.16}$$

where the expressions of R_o, R_i, H_o/R_o, H_i/R_i and d in terms of the thermodynamical variables N_f, R, c_o, c_i and τ are shown in Eq.(3.6), (3.7), (3.8), (3.11) and (3.12).

3.3 Results

Free energy formulas shown in Eq.(3.14), (3.15) and (3.16) dictate the self-assembly phase behaviours of PFS-b-PDMS in alkane solvents. If the material parameters x_1,

Lamella	N_f, c
Rod	N_f, N_r, c
Tube	N_f, R, τ, c_o, c_i

Table 3.1: Thermodynamical variables for lamellar, rodlike and tubular micelles.

x_2 and x_3 are known, the phase diagram which takes N_A, N_B and χ_{AS} as control parameters can be predicted. However, the determination of x_1, x_2 and x_3 based on first principle computations is not pursued in the current work. Rather, we would compute the phase diagrams in terms of qualitatively different (x_1, x_2, x_3) inputs and compare the results with experiments. On one hand, a reasonable range of (x_1, x_2, x_3) for PFS-b-PDMS/alkanes is suggested. On the other hand, since the model is universal for self-assembly of crystalline-coil copolymers in the solvents which are modest to poor for the coil blocks but nonsolvents for the crystalline blocks, we can classify this type of systems based on the different phase behaviours exhibited in these phase diagrams.

In what follows, we fix $N_B = 40$, which is consistent with the experiments we are interested in[9, 18]. We then compute the $\chi_{AS} - N_A$ phase diagrams in terms of different (x_1, x_2, x_3) inputs. According to Eq.(3.14), (3.15) and (3.16), the thermodynamical variables for the three morphologies are not the same (Table 3.1). To determine which morphology is thermodynamically stable for a specific phase point (χ_{AS}, N_A), we need to find the equilibrium values of the thermodynamical variables (TVs) which lead to the minimal F/kT. Then, we compare the minima of each morphology to determine the global minimum. There are two mathematically equivalent

methods to determine the equilibrium values of the TVs. Consider a free energy function in terms of n TVs: $F(y_1, y_2, \ldots, y_n)$. The first method is to solve the equilibrium equations $\partial F/\partial y_i = 0$. Generally, n coupled-equations would be given, where each one contains the n TVs. If more than one solution of these equations exist, we need further to find the one which gives the minimal free energy. The second method is simply to compute the free energies in terms of TVs of all possible values and find the minimum by comparison. In this work, the second method is used. The fact that physically N_f and N_r must be integers is followed.

To illustate how to obtain the phase diagram for given (x_1, x_2, x_3), we depict typical free energy curves for two types of transition sequences: $N_A - F$ curves at fixed χ_{AS} illustrating N_A-controlled transitions and $\chi_{AS} - F$ curves at fixed N_A illustrating χ_{AS}-controlled transitions. The calculation results show that there exist three types of morphological transitions: lamella-to-tube, tube-to-rod and lamella-to-rod transitions. Either of them can be induced by changing N_A or χ_{AS}. Below, we let the superscripts "LT", "TR" and "LR" represent the transition type. Four examples of free energy curves are shown in Figure 3.7, 3.8, 3.11 and 3.12.

Note in this chapter, when the value of the free energy in terms of some fixed parameters for one given morphology is mentioned, we have always performed the free energy minimization upon the other unfixed parameters. Since only the free energy differences are responsible for the micellar structure and distribution, the relative values of the free energies are used in the free energy curves which illustrate the morphological transitions. For each phase point, we take the free energy for the lamellar micelle as the zero point and use $\Delta F_{tube} = F_{tube} - F_{lamella}$ and $\Delta F_{rod} = F_{rod} - F_{lamella}$.

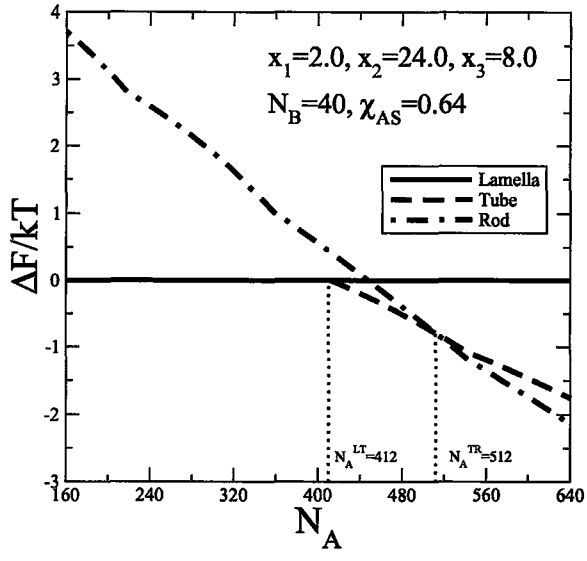

Figure 3.7: Free energy curves of lamellar, tubular and rodlike micelles illustrating N_A-controlled lamella-to-tube and tube-to-rod transitions. The intersection of the curves for lamellar and tubular micelles determines the crossover value $N_A^{LT} = 412$. The intersection of the curves for tubular and rodlike micelles determines the crossover value $N_A^{TR} = 512$.

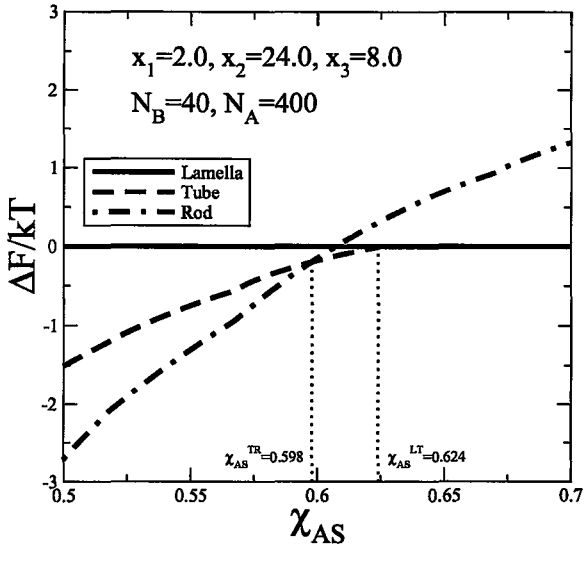

Figure 3.8: Free energy curves of lamellar, tubular and rodlike micelles illustrating χ_{AS}-controlled lamella-to-tube and tube-to-rod transitions. The intersection of the curves for lamellar and tubular micelles determines the crossover value $\chi_{AS}^{LT} = 0.624$. The intersection of the curves for tubular and rodlike micelles determines the crossover value $\chi_{AS}^{TR} = 0.598$.

The advantage of this treatment is that the contrast of the free energy curves for different morphologies is much more obvious than directly using the free energy values calculated from Eq.(3,14), (3.15) and (3.16).

In Figure 3.7 and 3.8, the free energy curves are partially the same for tubular and lamellar micelles due to an interesting relation between them. If we review the description of the tubular structure in subsection 3.2.1, lamellar micelles can be viewed as a limiting case ($R \rightarrow \infty$) of tubular micelles. From Figure 3.9 and 3.10, which show the tubular free energy in terms of $1/R$, we can find when N_A or χ_{AS} are close to the critical points N_A^{LT} or χ_{AS}^{LT}, there are two local free energy minima. One corresponds to $1/R = 0$ ($R \rightarrow \infty$) and the other corresponds to one finite R (around 10nm). However, for small enough N_A or large enough χ_{AS}, the minimum at $R \rightarrow \infty$ is unique and metastable finite-R tubes are not predicted. So, if the minimum at $R \rightarrow \infty$ is the global minimum, the free energy curves of lamellar and tubular micelles are the same. For the other case, i.e., a local minimum at a finite R is the global minimum, the free energy curves of tubular and lamellar micelles are different. The crossover point indicates the onset of the lamella-to-tube(finite R) transition, which is first-order.

In principle, lamellar micelles can also be viewed as a limiting case of rodlike micelles with $N_r \rightarrow \infty$ (of course, the word "rod" is not accurate any more if N_r is too large). However, restricted by the model, free energy curves of rodlike micelles in terms of $1/N_r$ can not be completely obtained. The effective model proposed in subsection 3.2.1 implicitly assumed that N_r is not too large. Eq.(3.3) shows that the effective core radius $R \propto N_r^{1/2}$. Thus, for large enough N_r, the result would contradict

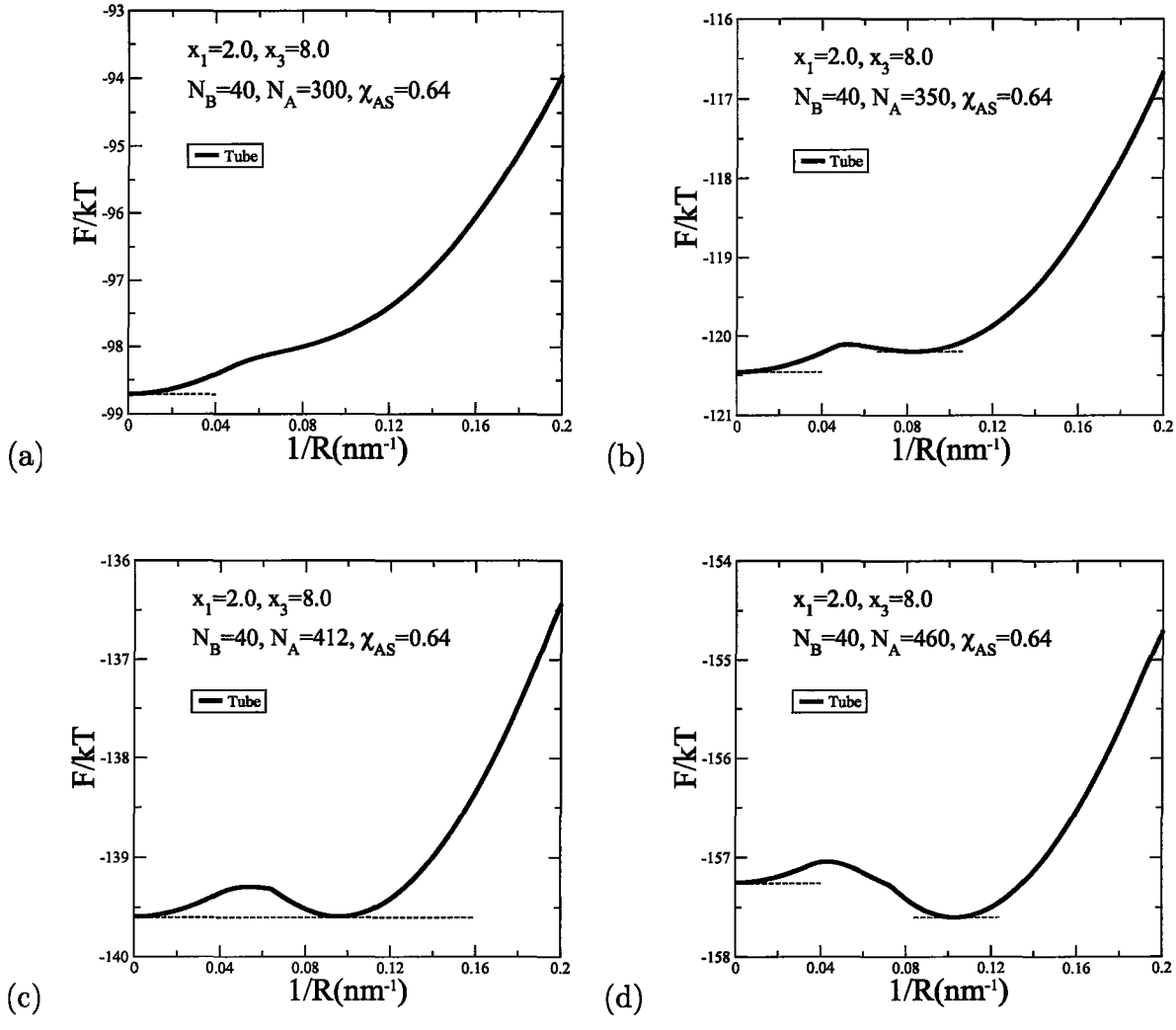

Figure 3.9: Free energy curves of tubular micelles in terms of $1/R$ illustrating N_A-controlled first-order lamella-to-tube(finite R) transition: (a)metastable finite-R tubes do not exist; (b)metastable finite-R tubes exist; (c)the local minima at $R \rightarrow \infty$ and at one finite R are equal, indicating the onset of the transition; (d)tubes are thermodynamically stable at one finite R.

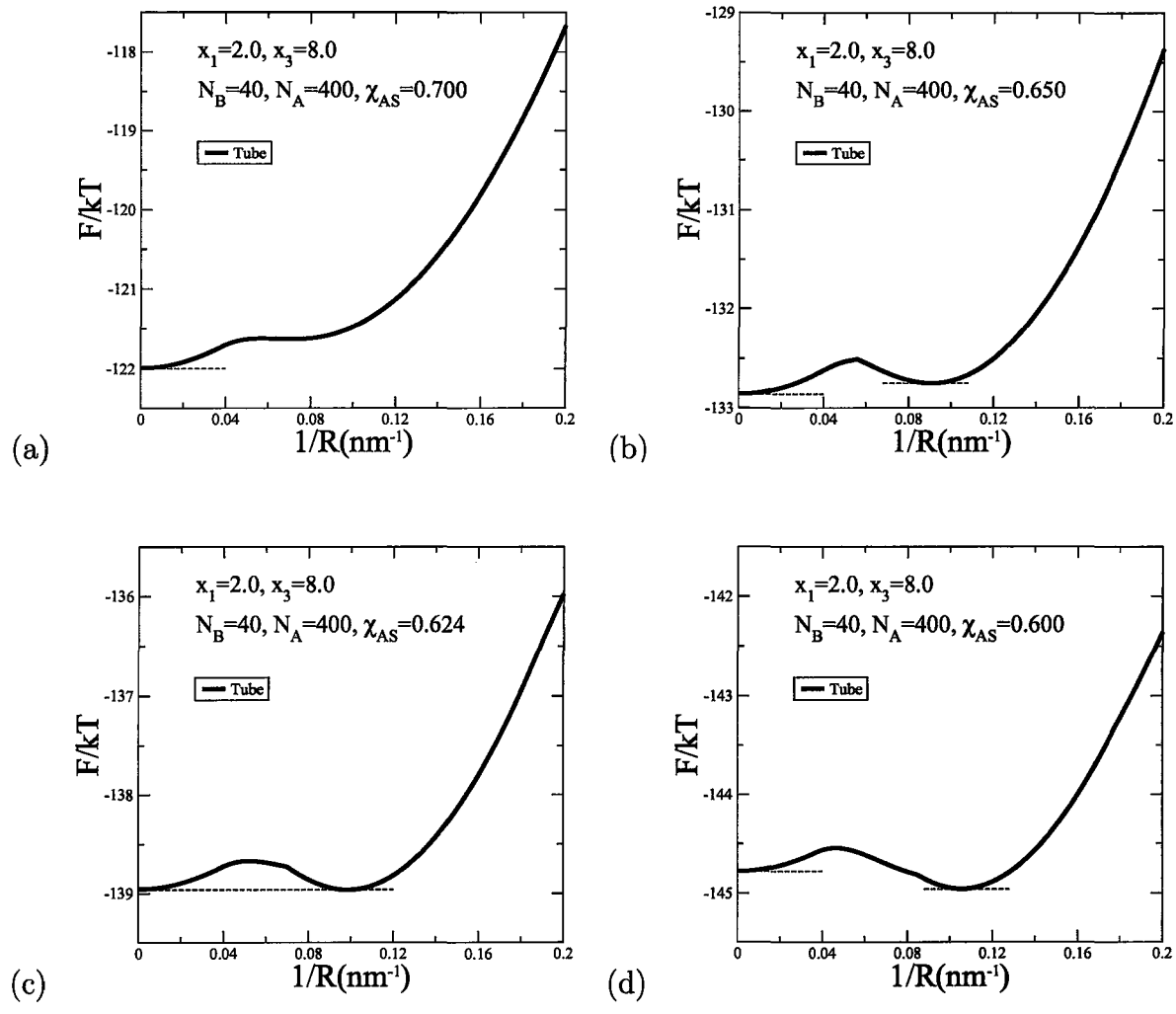

Figure 3.10: Free energy curves of tubular micelles in terms of $1/R$ illustrating χ_{AS}-controlled first-order lamella-to-tube(finite R) transition: (a)metastable finite-R tubes do not exist; (b)metastable finite-R tubes exist; (c)the local minima at $R \to \infty$ and at one finite R are equal, indicating the onset of the transition; (d)tubes are thermodynamically stable at one finite R.

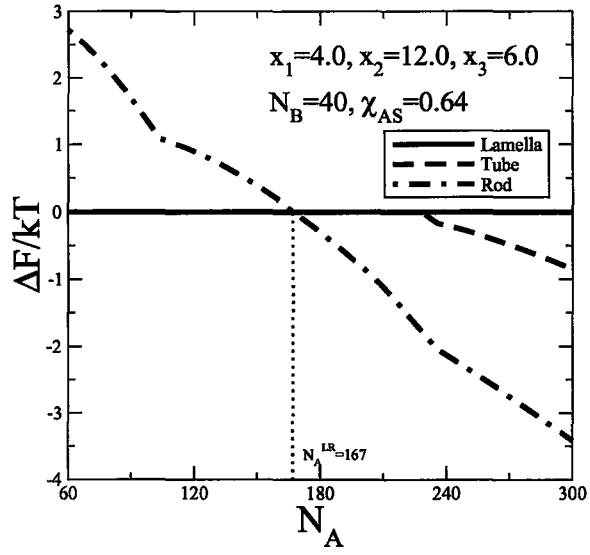

Figure 3.11: Free energy curves of lamellar, tubular and rodlike micelles illustrating N_A-controlled direct lamella-to-rod transition. The intersection of the curves for lamellar and rodlike micelles determines the crossover value $N_A^{LR} = 167$.

the precondition of the effective model in which the size of the long corona blocks dominates the core size so that the outer boundary of the corona is approximately a cylindrical surface. A more general theoretical model which is applicable for all values of N_r is desirable in this case. In section 3.4, where we discuss possible improvements of our theory, this issue will be analyzed.

For the current work, in most cases, the resulting effective radius R is smaller than the corona height H, which is consistent with the precondition of the effective model. The computation results show that a (local) free energy minimum at some finite N_r can always be found. Thus, at least in the framework of the effective model, a direct lamella-to-rod(finite N_r) transition, if existed, is also first-order. Besides, when lamellae are thermodynamically stable, metastable finite-N_r rods constantly exist. Note that when we depict the free energy curves, the lamellae are not treated

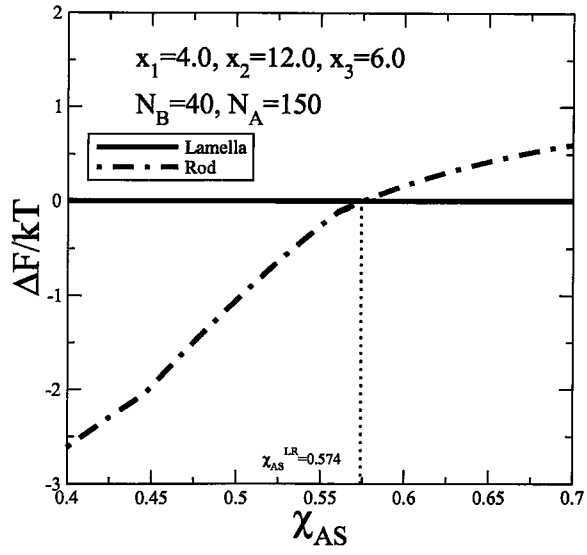

Figure 3.12: Free energy curves of lamellar, tubular and rodlike micelles illustrating χ_{AS}-controlled direct lamella-to-rod transition. The intersection of the curves for lamellar and rodlike micelles determines the crossover value $\chi_{AS}^{LR} = 0.574$. In this example, free energies of lamellar micelles ($R \to \infty$) are always lower than finite-R tubular micelles. Therefore, only two curves are seen.

as special rodlike micelles. We always use the data of the finite-N_r local minima to determine the curves. Therefore, except for the intersection, free energy curves of lamellar and rodlike micelles differ everywhere.

The free energy curves shown in figure 3.11 and 3.12 illustrate how direct lamella-to-rod transitions occur. The free energies of finite-R tubular micelles are larger than the free energies of either lamellar or rodlike micelles for all considered values of the control parameter N_A or χ_{AS}. In this case, the intersection of the free energy curves of lamellar and rodlike micelles determines the transition point.

One interesting feature of the free energy curves shown in Figure 3.7-3.12 is that the curves are not globally smooth. The underlying factor is the "jump" of the number of folds N_f. We explain in details below. The equlibrium value $N_{f,eq}$ for one

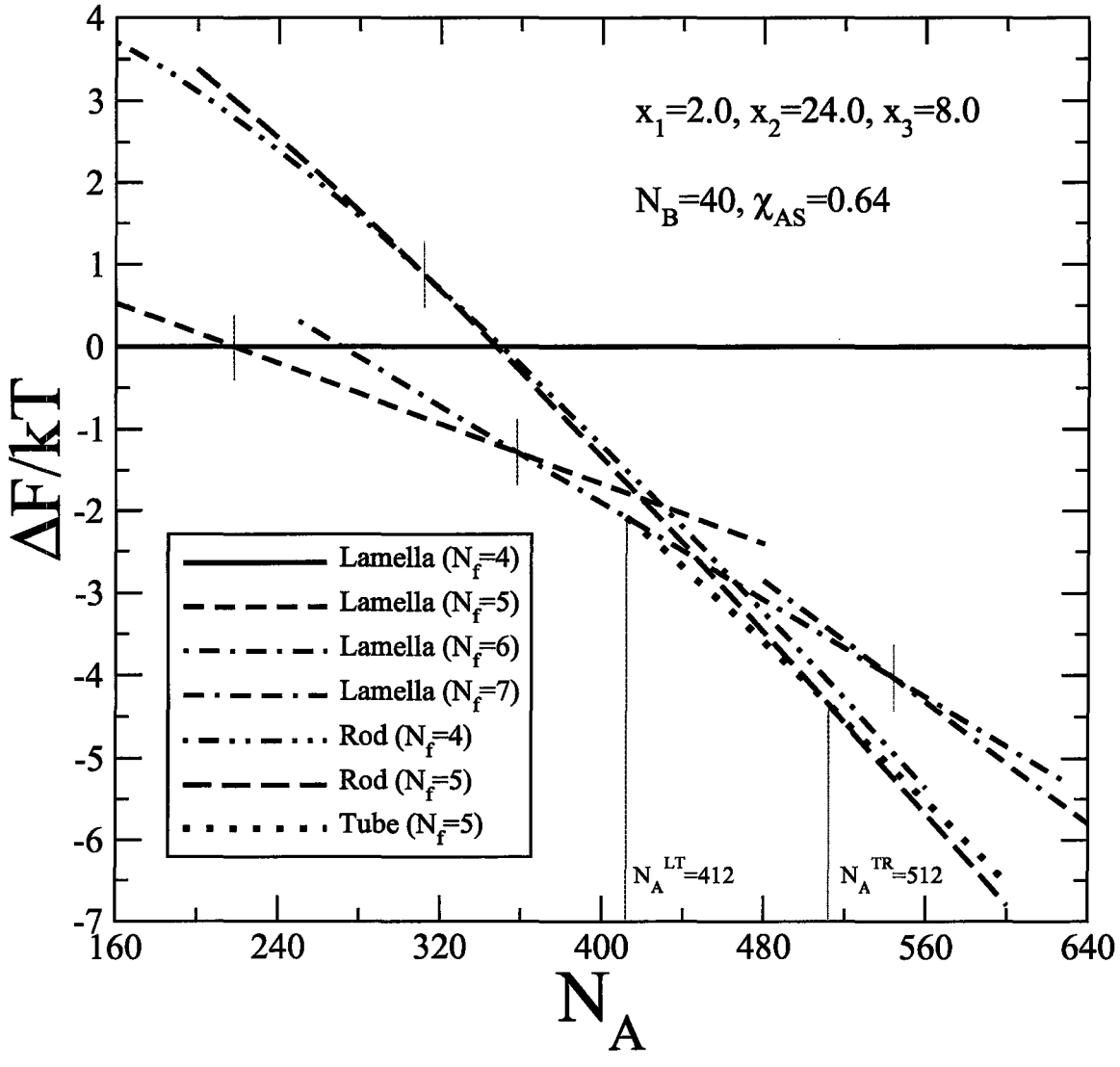

Figure 3.13: Free energy curves of lamellar, tubular and rodlike micelles at fixed N_f illustrating N_A-controlled lamella-to-tube, tube-to-rod transitions and the "jump" of the values of $N_{f,eq}$. The parameter input is the same as Figure 3.7. The $N_{f,eq}$ values for lamellar micelles change from 4 to 7 and for rodlike micelles change from 4 to 5 with increasing N_A. Therefore there are four "jump" points in this example (labeled in the diagram). The lamellar micelles with $N_{f,eq} = 6$ transit to tubular micelles with $N_{f,eq} = 5$ and the crossover value $N_A^{LT} = 412$. The tubular micelles with $N_{f,eq} = 5$ transit to rodlike micelles with $N_{f,eq} = 5$ and the crossover value $N_A^{TR} = 512$.

morphology is determined by minimizing the free energy. On one hand, larger N_A or smaller χ_{AS} would induce stronger swelling force of the corona blocks; on the other hand, larger N_f would lead to larger interface area per chain and make the unfavorable repulsion between adjacent coils of the corona blocks smaller. Therefore, $N_{f,eq}$ would increase when N_A is beyond some critical value or when χ_{AS} is lower than some critical value. In Figure 3.13, we depict the free energy curves at fixed N_f for each morphology to illustate this effect. The parameter input is the same as Figure 3.7. The lamellar free energy at $N_f = 4$ is taken as the zero point. For the whole range of N_A considered (160-640), the $N_{f,eq}$ values for lamellar micelles change from 4 to 7 and for rodlike micelles change from 4 to 5 with increasing N_A. Only for tubular micelles the value of $N_{f,eq}$ (=5) is not changed in the N_A range considered. The "jump" of the number of folds for lamellar and rodlike micelles are labeled in Figure 3.13. For the lamella-to-tube transition, it is that lamellar micelles with $N_{f,eq} = 6$ transit to tubular micelles with $N_{f,eq} = 5$ and the crossover value $N_A^{LT} = 412$. For the tube-to-rod transition, it is that tubular micelles with $N_{f,eq} = 5$ transit to rodlike micelles with $N_{f,eq} = 5$ and the crossover value $N_A^{TR} = 512$. In general, if we depict the free energy curves of the three morphologies based on the minimization upon all thermodynamical variables including N_f, as shown in Figure 3.7, 3.8, 3.11 and 3.12, the curves would not be globally smooth in the whole N_A or χ_{AS} range considered. Instead, they would be connected by several smooth segments, each of which corresponds to one value of $N_{f,eq}$. The values of $N_{f,eq}$ for each segment are different.

Above, we have shown how to determine the transition values N_A^{LT}, N_A^{TR}, N_A^{LR}, χ_{AS}^{LT}, χ_{AS}^{TR} and χ_{AS}^{LR} on the basis of free energy curves. This enables the deter-

mination of phase diagrams. Our calculations results suggest three types of phase diagrams. Examples for each are shown in Figure 3.14-3.16. The χ_{AS} range is chosen to be between 0.4 and 0.7. At 25°C, χ_{AS} has value of 0.64 for PDMS/decane[9]. At higher temperature, χ_{AS} would be smaller. So this range is appropriate for our interested systems. The main results are as follows:

(1) The two fundamental phases are lamellar and rodlike phases. For any (x_1, x_2, x_3) input and given χ_{AS}, if N_A is larger than one critical value N_A^r, rods are formed; if N_A is lower than another critical value N_A^l, lamellae are formed. In another word, it is predicted that universally in this type of systems, rods are thermodynamically stable in the large block ratio (N_A/N_B) limit while lamellae are thermodynamically stable in the low block ratio limit.

(2) The tubular phase is an intermediate phase and not predicted for all (x_1, x_2, x_3) inputs. For those phase diagrams in which the tubular phase exists (Figure 3.14 and 3.15), N_A^r is larger than N_A^l and tubular micelles are formed when $N_A^l < N_A < N_A^r$. In other words, N_A^l and N_A^r indicate the crossover from lamellar to tubular and tubular to rodlike micelles. Then in this case, we have $N_A^{LT} = N_A^l$ and $N_A^{TR} = N_A^r$. If $N_A^l = N_A^r$, i.e., tubular micelles are not formed (Figure 3.16), a direct lamella-to-rod transition is predicted. We then have $N_A^{LR} = N_A^l = N_A^r$.

(3) The phase behaviours are also greatly affected by the solvent property. For the χ_{AS} range in which lamella-to-tube, tube-to-rod or lamella-to-rod transitions exist, it is universal that the critical values N_A^{LT}, N_A^{TR} or N_A^{LR} shift to smaller values with better solvent property, i.e., smaller χ_{AS}. Moreover, for appropriate N_A, thermotropic lamella-to-tube, tube-to-rod or lamella-to-rod transitions are possible, which lead to

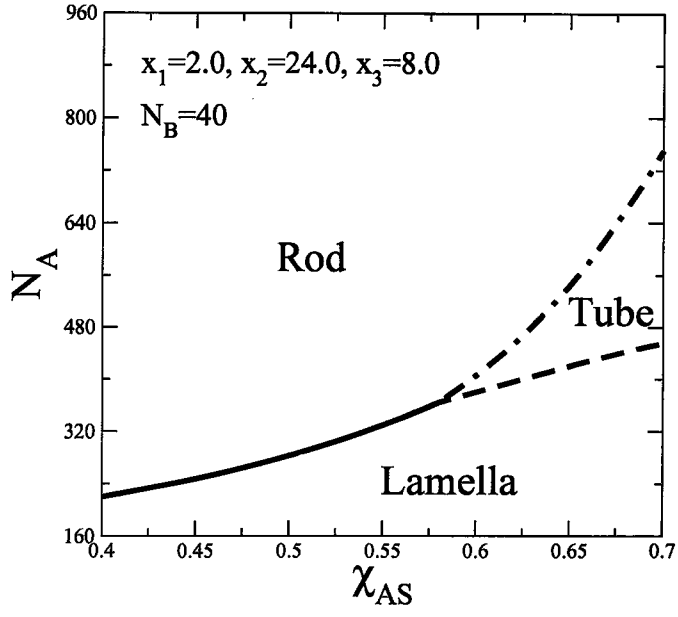

Figure 3.14: An example of the first-type of phase diagram: lamella-tube-rod phase diagram with a triple point.

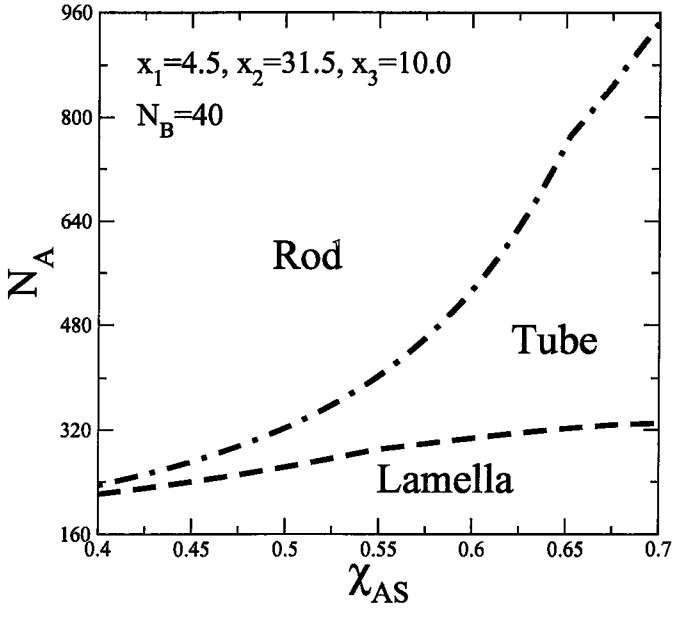

Figure 3.15: An example of the second-type of phase diagram: lamella-tube-rod phase diagram without a triple point.

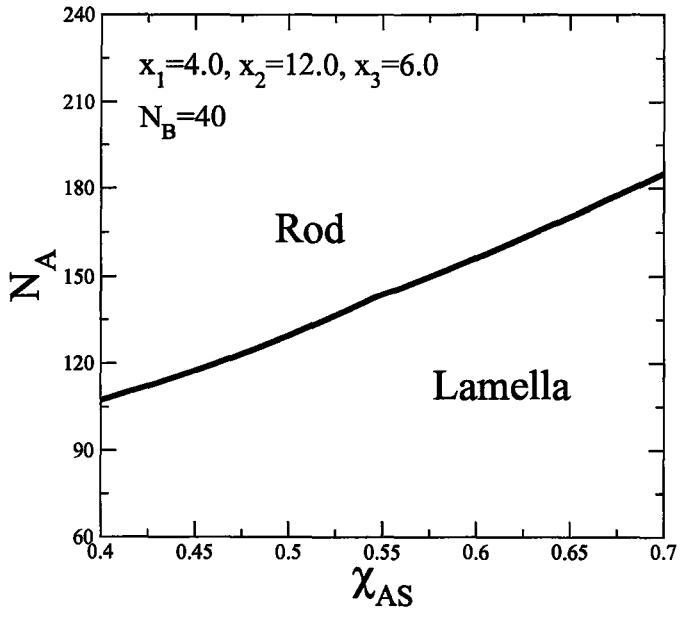

Figure 3.16: An example of the third-type of phase diagram: lamella-rod phase diagram.

the notations χ_{AS}^{LT}, χ_{AS}^{TR} and χ_{AS}^{LR}.

(4) It is confirmed that large enough block ratios would lead to non-lamellar morphologies. Moreover, it has been found that in some cases non-lamellar morphologies can be induced by simply improving the solvent property, with the polymerization degrees unchanged. The influence of the solvent property on crystalline-coil self-assembly was not discussed in the original work of VH.

(5) For some (x_1, x_2, x_3) inputs, an interesting triple point is predicted (Figure 3.14). Not all phase diagrams which include three phases have a triple point. For example, in the phase diagram shown in Figure 3.15, the lamella-to-tube and tube-to-rod transition lines do not intersect in the considered range of χ_{AS}. Note that although it seems the two lines would intersect at some χ_{AS} smaller than 0.4, the pre-condition of the existence of the crystalline-coil copolymer solutions should be kept

in mind. χ_{AS} is determined by the temperature for specific copolymer/solvent. Since the temperature must be below the melting temperature of the crystalline blocks and above some critical temperature below which the solutes or coil blocks become glassy, a bound of χ_{AS} is expected. Therefore, lamella-tube-rod phase diagrams without a triple point are possible.

In summary, the computation results show three types of phase diagrams, namely, lamella-tube-rod phase diagrams with or without a triple point and lamella-rod phase diagrams. For the first two, there exist remarkable lamella-tube-rod morphological transitions which can be induced by solely increasing the coil/crystalline block ratio or decreasing χ_{AS}.

The goal of the project presented in this chapter is to investigate the phase behaviours of the self-assembly of crystalline-coil copolymers in selective solvents for the coil blocks by taking PFS-b-PDMS/alkane as a model system. Although the theory enables quantitative investigations of the properties of aggregates (dictated by the equilibrium values of the TVs), such as the folding number, the solvent concentration of the corona, the distribution of the free ends of the corona blocks, the core size of the cylindrical micelles, and many others, a comprehensive study is still underway. A systematic summary of these properties is expected to be done in near future. Here, we briefly remark several intriguing features of tubular micelles:

(1) At a given phase point (χ_{AS}, N_A) in a tubular phase region, the equlibrium tube radius R_{eq} is determined by minimizing the free energy shown in Eq.(3.16). The computation results show that the values of R_{eq} at all phase points in a tubular phase region are in a narrow range. For most (x_1, x_2, x_3) inputs, the values of R_{eq} are in

the range of 5-15 nm.

(2) The asymmetric distribution of the corona blocks inside and outside the tubular micelle is another interesting feature. The equlibrium value of the number fraction of the coil blocks in the outer corona τ_{eq} is determined by minimizing the free energy shown in Eq.(3.16). For tubular micelles in the thermodynamical equlibrium, the number fraction of the coil blocks inside the tubes is therefore equal to $1 - \tau_{eq}$. The computation results show that in most cases, only 1-4% of the corona blocks are inside, indicating a remarkable asymmetry. The inner grafting density is thus much lower than the outer grafting density. In this work, we assume both the outer and inner corona blocks are strongly stretched to derive the conformational free energy (Appendix C). In the derivation, each coil block is characterized by a definite trajectory and the fluctuations of the coil blocks along these trajectories are ignored[23]. Strictly speaking, the strongly stretched condition for the inner corona block segments near the grafting interface is not satisfied. Upon making corrections of the conformational free energy by considering the fluctuation effect, the number fraction of the coil blocks in the inner corona should be larger than the results obtained in the current theoretical framework.

3.4 Discussions

In conclusion, our theory predicts three types of phase diagrams for the crystalline-coil copolymer self-assembly in selective solvents for the coil blocks. The results show that the intriguing tubular phase (nanotubes) is only an intermediate phase, while

lamellar and rodlike phases are respectively thermodynamically stable in the low and high coil/crystalline block ratio limits. To obtain quantitatively accurate phase diagram for a specific system (e.g., PFS-b-PDMS/alkanes), material parameters x_1, x_2 and x_3 need to be given. Below, we analyze the microscopic origins of these phenomenological parameters and suggest possible improvements of the current model.

The parameter x_1 is determined by two factors. The first is the energy per fold E_f. To compute its value, microscopic model incorporating energetic parameters at molecular level is required. In particular, accurate information of the conformations of the monomers around the fold is necessary. Such computation is therefore very challenging. The second is the crystalline/(coil+solvent) interface free energy. Even for the strong segregation system, the interface is still of finite width and can be viewed as an crossover layer dividing the pure crystalline-block region and the pure wet-brush(strongly stretched coil blocks immersed in solvents) region. The width of such a layer is balanced by two opposite trends: On one hand, the conformational entropy of the block segments confined in the layer would increase with the width; on the other hand, the unfavorable interactions between the crystalline segments and the solvents would also increase with the width. The value of the interface free energy is thus determined by the minimal free energy in terms of the optimal layer width. To quantify the interactions in the interface layer, two other Flory-Huggins parameters χ_{BS} and χ_{AB} are needed. However, since the history of PFS is very short, many parameters related to PFS are still lacking. To our knowledge, the Flory-Huggins parameters for PFS/PDMS and PFS/alkane are unknown.

The introduction of the parameter x_2 is due to the special morphological geom-

etry of the rodlike micelles. For the crystalline core which is in the shape of a long cuboid, there are two non-grafted lateral surfaces. The grafted coil blocks near the edges would extend away from the radial direction and are effectively "absorbed" by the non-grafted surfaces to reduce the unfavorable contacts between the crystalline blocks and the solvents (Figure 3.4). This costs the conformational free energy of the corona blocks and leads to large x_2 based on the effective model. An improved theory which enables accurate description of the block conformations throughout the corona is desirable. Let the axis of the rod be along the z-direction, we suggest the following approach. Assume the free-end positions (x_0, y_0) of the corona blocks satisfy a distribution function $g(x_0, y_0)$ and the trajectory of each chain is expressed as $\mathbf{r}(x, y; x_0, y_0)$. More generally, we consider the possible nonuniformity of the concentration of the block segments and let $\Phi(x, y)$ denote the distribution. Then in principle, computation based on the self-consistent field theory[25, 26] enables the derivation of g^*, $\mathbf{r}^*$ and Φ^* which minimize the free energy. Many one-dimensional cases, e.g., polymer brushes tethered on planar surfaces, have been treated in previous literatures. The suggested approach now is a two-dimensional case, which may demand additional computational techniques. Another advantage of this improved approach is that it enables the investigation of the intermediate corona profile between the two limits: cylindrical ($N_r \to 0$) and planar ($N_r \to \infty$). As discussed in section 3.3, the effective model fails to study such an intermediate case. The conclusion that a local minimum at some finite N_r always exists as the effective model predicted can be reliably tested by this new approach.

If the packing of the crystalline blocks are affected by the deformation of the core,

extra deformational energy would be induced, whose strength is characterized by the parameter x_3. The value of x_3 can be either measured by experiments or computed based on appropriate molecular model. Recently, a work combining experiments and computations to study the mechanical properties of PFS has been reported[27], which may benefit the estimation of the value of x_3 for PFS.

One of the most remarkable findings of Manners et al. was the thermotropic tube-to-rod transition[9]. For PFS_{40}-b-$PDMS_{480}$ in decane solvents, the TEM images showed that tubes are formed at 25°C and rods are formed at 50°C (Figure 3.2). Moreover, the transition between these two phases is reversible, indicating both phases are thermodynamically equilibrium phases. If the copolymer concentration Φ satisfies the relation $\Phi^* < \Phi \ll \Phi^{**}$ for the solution used in the TEM experiment, which is one precondition of our theory (see section 3.2), the χ_{AS}-N_A phase diagram of PFS_{40}-b-$PDMS_{N_A}$ in decane are then either of first-type or second-type. As shown in Figure 3.14 and 3.15, both phase diagrams predict the tube-to-rod transition observed in the system mentioned above. However, the "concentration problem" may really exist. According to the most recent work of Manners et al.[18], the tubular micelles shown in the TEM image are suspected to be a structural rearrangement or higher level of hierarchical self-assembly that takes place in concentrated solution. This suspicion is consistent with two facts. First, the data of the light-scattering measurements of dilute PFS_{40}-b-$PDMS_{480}$ at 25°C in decane indicate the self-assembled micelles are thin, rigid, rodlike structures rather than tubular structures. Secondly, solvent evaporation is indeed allowed when the TEM experiment is performed.

We end this chapter by discussions on the future research directions and chal-

lenges of studying PFS-b-PDMS self-assembly in alkane solvents. First, to best compare theories, information at more phase points are desirable. Since a theory which is completely constructed from first-principle computation is very challenging, introducing some phenomenological parameters, e.g., x_1, x_2 and x_3 in the current work, is more realistic. Comprehensive experimental information of the phase behaviours would help estimate the values of these parameters and in turn refine the predicted phase diagram. Secondly, these parameters can also be directly estimated based on complemental experiments and microscopic models. We have demonstrated the approaches of this type in the analysis of the origins of x_1, x_2 and x_3 shown above. Thirdly, the conditions of the experiments and the assumptions of the theories need to be consistent. Our theory would fail to predict the phase behaviours if the interactions between micelles become significant (concentrated solution). It seems the phase diagrams of PFS-b-PDMS/alkane at dilute and concentrated conditions are qualitatively different[18]. Thus, a new model is necessary for theoretically studying the concentrated regime. For experiments, since TEM images can directly show the morphology of the micelles, efforts are expected to be made by experimentalists to make sure the solution satisfies the dilute condition. Alternatively, if at the dilute condition doing other types of experiments in which the micellar morphology is not directly visible, reliable indirect methods are needed to determine the micellar morphology. Finally, there still remains many interesting subjects in this system which are beyond the scope of the current theoretical framework. For example, our models implicitly assumed an infinite length for both rodlike and tubular micelles. Although ignoring the block profile at two ends of the "cylinder" is appropriate to derive the

free energy per chain and analyze the phase behaviours, by a qualitative aggregation theory[19], such a profile is an important factor determining the distribution of the cylindrical lengths, while the polymer concentration Φ is another important factor. To give quantitative results of the subjects like this, new models are needed.

Appendix A

Calculation of $\langle r^2 \rangle_0$

Based on the constructed RIS ensemble, we can decompose the energy of an ideal PFDMS chain expressed in Eq.(2.2) as follows:

$$E(chain) = \sum_{i=4}^{3n+1} E_i(\Phi_{i-1}, \Phi_i) \tag{A.1}$$

where,

$$\begin{aligned} &E_{3i+1}(\Phi_{3i}, \Phi_{3i+1}) = E_{dimer}(\Phi_{3i}, \Phi_{3i+1}) \\ &E_{3j+2}(\Phi_{3j+1}, \Phi_{3j+2}) = 0 \\ &E_{3j+3}(\Phi_{3j+2}, \Phi_{3j+3}) = E'_{trimer}(\Phi_{3j+2}, \Phi_{3j+3}) \\ &i = 1, 2, \ldots, n; \quad j = 1, 2, \ldots, n-1 \end{aligned} \tag{A.2}$$

Within the RIS model[10], the partition function is written as

$$\begin{aligned} \mathrm{Z} &= \sum_{a_3=1}^{\nu_3} \cdots \sum_{a_{3n+1}=1}^{\nu_{3n+1}} \exp(-E(chain)/kT) \\ &= \sum_{a_3=1}^{\nu_3} \cdots \sum_{a_{3n+1}=1}^{\nu_{3n+1}} U_3(a_3, a_4) \ldots U_{3n}(a_{3n}, a_{3n+1}) \end{aligned} \tag{A.3}$$

where,

$$U_i(a_i, a_{i+1}) = \exp(-E_i(\Phi_i(a_i), \Phi_{i+1}(a_{i+1}))/kT) \tag{A.4}$$

if the combination $(\Phi_i(a_i), \Phi_{i+1}(a_{i+1}))$ are included in the ensemble. Otherwise, $U_i(a_i, a_{i+1}) = 0$.

In Eq.(A.3), the values of $\nu_3, \nu_4, \ldots, \nu_{3n+1}$ are determined as follows: $\nu_i = 6$ if the associated angle Φ_i is in a dimer pair or $\nu_i = 20$ if the associated angle is a trimer angle. For the former case, $\Phi_i(1)$ to $\Phi_i(6)$ = 20, -20, 145, -145, 110 and -110 (unit: °), respectively; for the latter case, $\Phi_i(1)$ to $\Phi_i(20)$ = 62, -62, 64, 64, 73, -73, 75, -75, 80, -80, 83, -83, 88, -88, 90, -90, 91, -91, 101 and -101 (unit: °), respectively.

In general, the thermal average of any geometrical quantity A of an ideal PFS chain can be written as

$$\begin{aligned} \langle A \rangle_0 = \mathrm{Z}^{-1} \sum_{a_3=1}^{\nu_3} \cdots \sum_{a_{3n+1}=1}^{\nu_{3n+1}} & A(\{\Phi_i(a_i)\}) \\ & \times U_3(a_3, a_4) \ldots U_{3n}(a_{3n}, a_{3n+1}) \end{aligned} \tag{A.5}$$

It is convenient to transform the summations into matrix multiplications. The statistical weight matrices (U-matrices) are

$$U_3 = U_6 = \cdots = U_{3n} = U_a$$

$$= \begin{bmatrix} 0 & 0 & 1 & 0 & 0 & 0 \\ 0 & 0 & 0 & 1 & 0 & 0 \\ 1 & 0 & 0 & 0 & 0 & 0 \\ 0 & 1 & 0 & 0 & 0 & 0 \\ 0 & 0 & 0 & 0 & x & 0 \\ 0 & 0 & 0 & 0 & 0 & x \end{bmatrix} \tag{A.6}$$

$$U_4 = U_7 = \cdots = U_{3n-2} = U_b$$

$$= \begin{bmatrix} 0 & 0 & 0 & 0 & 0 & 1 & 1 & 0 & 0 & 1 & 0 & 0 & 1 & 0 & 1 & 1 & 0 & 0 & 1 & 0 \\ 0 & 0 & 0 & 0 & 1 & 0 & 0 & 1 & 1 & 0 & 0 & 0 & 0 & 1 & 1 & 1 & 0 & 0 & 0 & 1 \\ 0 & 1 & 0 & 1 & 0 & 1 & 0 & 1 & 0 & 0 & 1 & 1 & 0 & 0 & 0 & 0 & 1 & 0 & 1 & 0 \\ 1 & 0 & 1 & 0 & 1 & 0 & 1 & 0 & 0 & 0 & 1 & 1 & 0 & 0 & 0 & 0 & 0 & 1 & 0 & 1 \\ 0 & 0 & 0 & 1 & 0 & 0 & 0 & 0 & 0 & 1 & 0 & 0 & 0 & 0 & 0 & 0 & 0 & 1 & 0 & 0 \\ 0 & 0 & 1 & 0 & 0 & 0 & 0 & 0 & 1 & 0 & 0 & 0 & 0 & 0 & 0 & 0 & 1 & 0 & 0 & 0 \end{bmatrix} \tag{A.7}$$

$$U_5 = U_8 = \cdots = U_{3n-1} = U_c$$

$$= \begin{bmatrix} 0 & 0 & 0 & y_6 & 0 & 0 \\ 0 & 0 & y_6 & 0 & 0 & 0 \\ 0 & 0 & 0 & y_1 & 0 & y_1 \\ 0 & 0 & y_1 & 0 & y_1 & 0 \\ 0 & y_3 & 0 & y_3 & 0 & 0 \\ y_3 & 0 & y_3 & 0 & 0 & 0 \\ y_4 & 0 & 0 & y_4 & 0 & 0 \\ 0 & y_4 & y_4 & 0 & 0 & 0 \\ 0 & y_9 & 0 & 0 & 0 & y_9 \\ y_9 & 0 & 0 & 0 & y_9 & 0 \\ 0 & 0 & y_7 & y_7 & 0 & 0 \\ 0 & 0 & y_7 & y_7 & 0 & 0 \\ y_8 & 0 & 0 & 0 & 0 & 0 \\ 0 & y_8 & 0 & 0 & 0 & 0 \\ y_{10} & y_{10} & 0 & 0 & 0 & 0 \\ y_{10} & y_{10} & 0 & 0 & 0 & 0 \\ 0 & 0 & y_2 & 0 & 0 & y_2 \\ 0 & 0 & 0 & y_2 & y_2 & 0 \\ y_5 & 0 & y_5 & 0 & 0 & 0 \\ 0 & y_5 & 0 & y_5 & 0 & 0 \end{bmatrix} \tag{A.8}$$

where, $x = \exp(-(1.0\text{Kcal/mol} + \Delta E)/kT)$ and $y_i = \exp(-\varepsilon_i/kT)$. ε_i are shown in Table 2.3. For convenience, we let

$$U_1 = [1], \quad U_2 = J^T = \begin{bmatrix} 1 & 1 & 1 & 1 & 1 & 1 \end{bmatrix} \tag{A.9}$$

The partition function is then written as a matrix multiplication

$$\mathrm{Z} = U_2(U_a U_b U_c)^{n-1} U_a J \tag{A.10}$$

and

$$\begin{aligned} &\langle r^2 \rangle_0 \\ &= \left\langle \sum_{1 \le i \le j \le 3n+1} \mathbf{l}_i \bullet \mathbf{l}_j \right\rangle_0 \\ &= 2\mathrm{Z}^{-1} \begin{bmatrix} U & (U \bigotimes L^T)\|T\| & (l^2/2)U \\ 0 & (U \bigotimes I_3)\|T\| & U \bigotimes L \\ 0 & 0 & U \end{bmatrix}_1^{(3n)} \begin{bmatrix} (l_a^2/2)I_6 \\ I_6 \bigotimes L_a \\ I_6 \end{bmatrix} J \end{aligned} \tag{A.11}$$

Eq.(A.11) is obtained by the standard approach presented in details in Flory's monograph[10]. The pseudobond angles needed in determining the coordinate transform matrices $\{T_i\}$ are shown in Table 2.2 (boldface fonts).

Appendix B

Calculation of $\langle R_g^2 \rangle_0$

By the definition given in section 2.4, we label the iron atoms as iron 0, iron 1, ..., iron n following the chain sequence and let R_{ij} denotes the distance between iron i and iron j. Then

$$\begin{aligned} R_{ij}^2 &= (\sum_{k=3i+1}^{3j+1} \mathbf{l}_k) \bullet (\sum_{p=3i+1}^{3j+1} \mathbf{l}_p) \\ &= \sum_{k=3i+1}^{3j+1} \mathbf{l}_k^2 + 2 \sum_{3i<k<p\leq 3j+1} \mathbf{l}_k \bullet \mathbf{l}_p \end{aligned} \tag{B.1}$$

Note that the length of l_{3i+1} and l_{3j+1} is assigned as $l_a/2$ in Eq.(B.1) because the iron atom is at the middle of the Pc-Pc bond. All other notations are the same with Eq.(A.11). Use Lagrange's theorem

$$R_g^2 = (n+1)^{-2} \sum_{0\leq i<j\leq n} R_{ij}^2 \tag{B.2}$$

by incorporating the the expressions of $\langle R_{ij}^2 \rangle_0$ in terms of matrix computations, which are analogous to $\langle r^2 \rangle_0$, we can express $\langle R_g^2 \rangle_0$ by performing computation of larger size

matrices.

$$\left\langle R_g^2 \right\rangle_0 = 2(n+1)^{-2}\mathrm{Z}^{-1} \begin{bmatrix} \mathcal{U}_0 & \mathcal{F}_0 & 0 \end{bmatrix} \begin{bmatrix} \mathcal{U} & \mathcal{IF} & 0 \\ 0 & \mathcal{F} & \mathcal{GU} \\ 0 & 0 & \mathcal{U} \end{bmatrix}^{n-1} \begin{bmatrix} 0 \\ \mathcal{G} \\ I_6 \end{bmatrix} J \tag{B.3}$$

where,

$$\mathcal{U}_0 = U_2 U_a,\ \mathcal{F}_0 = U_2 F_1 F_2 F_a,\ \mathcal{U} = U_b U_c U_a,\ \mathcal{F} = F_b F_c F_a$$

$$\mathcal{I} = \begin{bmatrix} I_6 & 0 & 0 \end{bmatrix},\ \mathcal{G} = \begin{bmatrix} (l_a^2/8) I_6 \\ (1/2) I_6 \bigotimes L_a \\ I_6 \end{bmatrix} \tag{B.4}$$

and

$$F_1 = \begin{bmatrix} 1 & L_a^T \|T\|_1 & l_a^2/2 \\ 0 & \|T\|_1 & L_a \\ 0 & 0 & 1 \end{bmatrix} \tag{B.5}$$

$$F_2 = \begin{bmatrix} U_2 & (U_2 \bigotimes L_b^T)\|T\|_c & (l_b^2/2) U_2 \\ 0 & (U_2 \bigotimes I_3)\|T\|_c & U_2 \bigotimes L_b \\ 0 & 0 & U_2 \end{bmatrix} \tag{B.6}$$

$$F_a = \begin{bmatrix} U_a & (U_a \bigotimes L_b^T)\|T\|_a & (l_b^2/2) U_a \\ 0 & (U_a \bigotimes I_3)\|T\|_a & U_a \bigotimes L_b \\ 0 & 0 & U_a \end{bmatrix} \tag{B.7}$$

$$F_b = \begin{bmatrix} U_b & (U_b \bigotimes L_a^T)\|T\|_b & (l_a^2/2)U_b \\ 0 & (U_b \bigotimes I_3)\|T\|_b & U_b \bigotimes L_a \\ 0 & 0 & U_b \end{bmatrix} \tag{B.8}$$

$$F_c = \begin{bmatrix} U_c & (U_c \bigotimes L_b^T)\|T\|_c & (l_b^2/2)U_c \\ 0 & (U_c \bigotimes I_3)\|T\|_c & U_c \bigotimes L_b \\ 0 & 0 & U_c \end{bmatrix} \tag{B.9}$$

Appendix C

Conformational Free Energy of Corona Blocks

Common examples of strongly segregated systems are seen in block-copolymer microdomains and micelles and also end-grafted polymer layers (polymer brushes), where the amorphous polymer blocks are highly extended (strongly-stretched). In 1985, Semenov formulated an analytical theory to compute the conformational free energy of strongly-stretched amorphous polymer blocks, originally in discussing diblock-copolymer melts[23]. Compared with the earlier works of Alexander[28] and de Gennes[29], where all corona blocks were assumed to be stretched to the same degree, Semenov's approach gives a more realistic picture that the free ends are broadly distributed across the corona layer. In this appendix, we generalize Semenov's approach to the corona blocks of the self-assembled diblock-copolymer micelles, where solvents and amorphous blocks coexsit. Since by mean-field theory, we have assumed the block volume fraction throughout the corona is a constant c as stated in subsection 3.2.1,

this generalization is straightforward.

In what follows, we consider five types of corona geometries:

(1) Planar grafted surface with two coronas of the height H.

(2,3) Cylindrical grafted surface with radius R. The corona blocks protrude outward or inward. The corona height is H. For the latter case, $H \leq R$ is physically required. The interface area per chain is α.

(4,5) Spherical grafted surface with radius R. The corona blocks protrude outward or inward. The corona height is H. For the latter case, $H \leq R$ is physically required. The interface area per chain is α.

We only meet (1), (2) and (3) in current work. However, since (4,5) correspond to another two common types of micelles: spheres and vesicles, we would expect the related results are useful elsewhere. Again, although not all geometries described above were discussed by Semenov, the generalization is straightforward.

In what follows, corona blocks are referrd as A-blocks. By the "strongly-stretched" condition (SSC), we assume the line connecting the grafted and free ends of one A-block is along the radius of the grafted surface and let r_0 denote the distance between the free end and the surface. We also let $g(r_0)dr_0$ be the number of blocks whose free ends lie in the interval dr_0. By the Gaussian chain model, the conformational free energy F_c of the corona blocks can be expressed as:

$$F_c/kT = \frac{3}{2\langle R^2\rangle_0}\int_0^H dr_0 g(r_0)\int_0^1 ds\left[\frac{\partial \mathbf{r}(s,r_0)}{\partial s}\right]^2 \qquad \text{(C.1)}$$

where, $\langle R^2\rangle_0$ is the mean-square ene-to-end distance of the ideal block, which equals to $N_A l_{K_A} a_A$. $\mathbf{r}(s,r_0)$ describes the three-dimensional trajactory of the block whose

free end is r_0 from the surface, where s is an arc length variable running from 0 to 1 along the block contour[30].

Eq.(C.1) can be simplified by an approximation based on SSC. Since the contour of the stretched block is mainly along the raduis, we only retain the radial component of $\mathbf{r}$ and by a variable transformation, denote it as $r(n, r_0)$, where n runs from 0 (grafted end) to N_A (free end). This leads to:

$$\begin{aligned} F_c/kT &= \frac{3}{2l_{K_A}a_A}\int_0^H dr_0 g(r_0)\int_0^{N_A} dn\left[\frac{\partial r(n,r_0)}{\partial n}\right]^2 \\ &= \frac{3}{2l_{K_A}a_A}\int_0^H dr_0 g(r_0)\int_0^{r_0} dr E(r,r_0) \end{aligned} \tag{C.2}$$

where we have used $E(r, r_0)$ to denote the local extension $\partial r(n, r_0)/\partial n$ in Eq.(C.2). For $g(r_0)$ and $E(r, r_0)$, $0 \le r \le r_0 \le H$ is required.

Two additional conditions are imposed on the unknown functions $g(r_0)$ and $E(r, r_0)$:

$$\int_0^{r_0} \frac{dr}{E(r,r_0)} = N_A \tag{C.3}$$

$$\int_r^H \frac{g(r_0)dr_0}{E(r,r_0)} = \frac{S_(r)c}{a_A^3} \tag{C.4}$$

where,

$$S(r) = \begin{cases} 2 & \text{for (1), unit-area planar surface} \\ 2\pi(R \pm r) & \text{for (2) and (3), unit-length cylindrical surface} \\ 4\pi(R \pm r)^2 & \text{for (4) and (5)} \end{cases}$$

The minimization of Eq.(C.2) under the additional conditions Eq.(C.3) and (C.4) lead to the solution:

$$E(r, r_0) = \frac{\pi}{2N_A}\left(r_0^2 - r^2\right)^{1/2} \tag{C.5}$$

Substitute Eq.(C.5) into Eq.(C.4) and let $t = r_0^2/H^2$, $u = r^2/H^2$,

$$g(r_0) = H^{d-2} r_0 h_d(t)/N_A \tag{C.6}$$

where $d = 1$, 2 and 3 respectively correspond to (1), (2,3) and (4,5), we get:

$$\int_1^u dt \frac{h_d(t)}{(t-u)^{1/2}} = \frac{\pi}{H^{d-1}} S_d(u) \tag{C.7}$$

where,

$$\begin{cases} S_1(u) = & 2 \\ S_2(u) = & 2\pi R \pm 2\pi H u^{1/2} \\ S_3(u) = & 4\pi R^2 \pm 8\pi R H u^{1/2} + 4\pi H^2 u \end{cases}$$

The solutions of the integral equation Eq.(C.7) are:

$$h_1(t) = \frac{2c}{a_A^3} (1-t)^{-1/2} \tag{C.8}$$

$$h_2(t) = \frac{2\pi c}{a_A^3} (1-t)^{-1/2} \left(\pm 1 + \frac{R}{H} \right) \mp \frac{2\pi c}{a_A^3} \tanh^{-1} (1-t)^{1/2} \tag{C.9}$$

$$\begin{aligned} h_3(t) \quad = \quad & \frac{4\pi R^2 c}{H^2 a_A^3} (1-t)^{-1/2} + \frac{4\pi c}{a_A^3} (2t-1) (1-t)^{-1/2} \pm \\ & \frac{8\pi R c}{H a_A^3} \left[(1-t)^{1/2} - \tanh^{-1} (1-t)^{1/2} \right] \end{aligned} \tag{C.10}$$

The forms of $g(r_0)$ are easily obtained by substituting $h_d(t)$ in Eq.(C.6).

Finally, upon substituting solved $g(r_0)$ and $E(r, r_0)$ into Eq.(C.2) and using simple volume conservation conditions, we can determine the conformational free energy f_c per corona block. Expressed in the unit of kT, for (1), (2,3) and (4,5) respectively, we have:

$$f_c = \frac{\pi^2 H^2}{8 N_A l_{K_A} a_A} \tag{C.11}$$

$$f_c = \frac{\pi^2 H^3 c}{8 N_A^2 l_{K_A} a_A^4} \left[1 \pm \frac{3}{4} \left(\frac{H}{R} \right) \right] \alpha \tag{C.12}$$

$$f_c = \frac{\pi^2 H^3 c}{8 N_A^2 l_{K_A} a_A^4} \left[1 \pm \frac{3}{2} \left(\frac{H}{R} \right) + \frac{3}{5} \left(\frac{H}{R} \right)^2 \right] \alpha \tag{C.13}$$

Bibliography

[1] Foucher, D.; Tang B.; Manners, I. *J. Am. Chem. Soc.* **1992**, *114*, 6246

[2] Kulbaba, K.; Manners, I. *Macromol. Rapid Commun.* **2001**, *22*, 711

[3] Manners, I. *Synthetic Metal-Containing Polymers*; WILEY-VCH: Weinheim, 2004

[4] Rulkens, R.; Resendes, A.; Verma, A.; Manners, I.; Murti, K.; Fossum E.; Miller, P.; Matyjaszewski, K. *Macromolecules* **1997**, *30*, 8165

[5] Massey, J. A.; Kulbara, K.; Winnik, M. A.; Manners, I. *J. Polym. Sci. Part B Polym. Phys.* **2000**, *38*, 3032

[6] Massey, A. J.; Temple, K.; Cao, L.; Rharbi, Y.; Raez, J.; Winnik, A. M.; Manners, I. *J. Am. Chem. Soc.* **2000**, *122*, 11577

[7] Raez, J.; Manners, I.; Winnik, A. M. *J. Am. Chem. Soc.* **2002**, *124*, 10381

[8] Raez, J.; Manners, I.; Winnik, A. M. *Langmuir* **2002**, *18*, 7229

[9] Raez, J.; Tomba J. P.; Manners, I.; Winnik, A. M. *J. Am. Chem. Soc.* **2003**, *125*, 9546

[10] Flory, P. J. *Statistical Mechanics of Chain Molecules*; Wiley: New York, 1969

[11] Mattice, W. L.; Suter, U. W. *Conformational Theory of Large Molecules. The Rotational Isomeric State Model in Macromolecular Systems*; Wiley: New York, 1994

[12] Rehahn, M.; Mattice, W. L.; Suter, U. W. *Adv. Polym. Sci.* **1997**, *131/132*, 1

[13] Barlow, S.; Rohl, A. L.; Shi, S.; Freeman, M.; O'Hare, D. *J. Am. Chem. Soc.* **1996**, *118*, 7578

[14] Rulkens, R.; Lough, A.; Manners, I.; Lovelace, S.; Grant, C.; Geiger, W. *J. Am. Chem. Soc.* **1996**, *118*, 12683; *Summary of Structure Determination of* 7_5(unpublished)

[15] de Gennes, P. G. *Scaling Concepts in Polymer Physics*; Cornell University Press: Ithaca, New York, 1979

[16] Mattice, W. L.; Helfer, C. A.; Sokolov, A. P. *Macromolecules* **2003**, *36*, 9924

[17] Lammertink, R.; Hernpenius, M.; Thormas, E.; Vancso, G. *J. Polym. Sci. Part B Polym. Phys.* **1999**, *37*, 1909

[18] Guerin, G.; Raez, J.; Manners, I.; Winnik, A. M. *Macromolecules* **2005**, *38*, 7819

[19] Jones, R. A. L. *Soft Condensed Matter*; Oxford University Press: New York, 2002

[20] Vilgis, T.; Halperin, J. *Macromolecules* **1991**, *24*, 2090

[21] Dimarzio, E. A.; Guttman, G. M.; Hoffman, J. D. *Macromolecules* **1980**, *13*, 1194

[22] Safran, S. A. *Statistical Thermodynamics of Surfaces, Interfaces and Membranes*; Westview Press: Boulder, Colorado, 2003

[23] Semenov, A. N. *Sov. Phys. JETP* **1985**, *61*, 733

[24] Mark, J. E. *Polymer Data Handbook*; Oxford University Press: New York, 1999

[25] Matsen, M. W. *J. Chem. Phys.* **2002**, *117*, 2351

[26] Kawakatsu, T. *Statistical Physics of Polymers*; Springer-Verlag: Berlin, 2004

[27] Smith, C. R.; Tan, K. H.; Evans, K. E.; Resendes, R.; Bartole-Scott A.; Manners I. *J. Polym. Sci. Part B Polym. Phys.* **2005**, *43*, 2280

[28] Alexander, S. *J. Phys. (Paris)* **1977**, *38*, 983

[29] de Gennes, P. G. *J. Phys. (Paris)* **1976**, *37*, 1443

[30] Doi, M.; Edwards, S. F. *The Theory of Polymer Dynamics*; Oxford University Press: New York, 1986